2018

Fracture and deformation of soft materials and structures

Zhuo Ma
Iowa State University

Fracture and deformation of soft materials and structures

by

Zhuo Ma

A dissertation submitted to the graduate faculty

in partial fulfillment of the requirements for the degree of

DOCTOR OF PHILOSOPHY

Major: Engineering Mechanics

Program of Study Committee:
Wei Hong, Co-major Professor
Ashraf Bastawros, Co-major Professor
Pranav Shrotriya
Liang Dong
Liming Xiong

The student author, whose presentation of the scholarship herein was approved by the program of study committee, is solely responsible for the content of this dissertation. The Graduate College will ensure this dissertation is globally accessible and will not permit alterations after a degree is conferred.

Iowa State University

Ames, Iowa

2018

TABLE OF CONTENTS

Page

LIST OF FIGURES iv

ACKNOWLEDGMENTS x

ABSTRACT xi

CHAPTER 1. INTRODUCTION 1
1.1 Soft Materials and Structures 1
1.2 Applications of Soft Materials and Structures 2
1.3 Fracture of Rubber 3
1.4 Dissertation Outline 4
1.5 References 6

CHAPTER 2. PHASE FIELD MODEL AND FRACTURE OF SOFT ELASTIC FOAM 8
2.1 Introduction 8
2.2 Phase-field model of fracture 11
2.3 Energy dissipation and numerical implementation 14
2.4 Results and discussion 19
2.5 Conclusion 29
2.6 References 30

CHAPTER 3. HIGHLY STRETCHABLE DOUBLE-NETWORK COMPOSITE AND ITS THEORY 32
3.1 Introduction 32
3.2 Experimental 35
3.2.1 Sample fabrication and testing 35
3.2.2 Uniaxial tension 36
3.2.3 Fracture tests 40
3.3 Theory 44
3.4 Conclusions 51
3.5 References 52

CHAPTER 4. A MAGNETIC DOUBLE-NETWORK COMPOSITE CAPABLE OF LARGE RECOVERABLE DEFORMATION 55
4.1 Introduction 55
4.2 Experimental setup and results 57
4.3 Theoretical 62
4.4 Discussion 70
4.5 References 71

CHAPTER 5. FRACTURE OF DOUBLE NETWORK GEL 73
5.1 Introduction 73
5.2 Transformation toughening theory 75
5.3 Phase field model of double network gel 78
5.4 Results and discussion 83
5.5 Conclusion 89
5.6 References 89

CHAPTER 6. CONCLUSION 91

LIST OF FIGURES

Page

Figure 2.1. The rupture and retraction process of a ligament (or cell wall) in a foam structure. Because of its slenderness, a soft filament will tend to buckle or coil and could not effectively transduce energy. 15

Figure 2.2. Sketch of the loading conditions for the foam structures 18

Figure 2.3. (a) Part of the 2D honeycomb foam structure being simulated. (b) The calculated deformation and damage fields of a honeycomb structure, during the propagation of a preexsting crack. The shades represent the dimensionless strain energy density W/W_c. The crack profile is indicated schematically by the dash line, which goes through the the transition zone from the intact to the fully damaged regions in terms of ϕ. The deformation is shown to scale, and only part of the structure near the crack tip is shown. The actual computational domain is much larger than that shown to circumvent size-effect. 19

Figure 2.4. (a) Undeformed coordinates of the ligaments as a function of the times of rupture. The line is the best linear fit. The slope indicates the dimensionless crack velocity. (b) Dimensionless fracture energy (energy-release rate) Γ/rW_c as a function of the dimensionless crack velocity v/rmW_c. The line is the best linear fit, and the vertical intercept shows the quasi-static fracture energy of the soft foam. 20

Figure 2.5. Calculated fracture energy of the hexagonal soft foams versus (a) the normalized ligament length l/r at constant volume fraction $\psi = 9\%$, and (b) the volume fraction of the solid phase ψ at constant ligament length $l/r = 4.2$. Two different orientations are simulated as indicated by the insets (with horizontal cracks). 21

Figure 2.6. Damage patterns of hexagonal soft foams in (a) “zigzag” and (b) “armchair” orientations. The color scale represents the damage variable ϕ, plotted in the undeformed geometry. The dash curves show the approximate paths of crack propagation. 23

Figure 2.7. Geometric effect on the fracture energy of soft foams. The geometries and orientations are represented by the sketch insets, with cracks running horizontally. 24

Figure 2.8. (a) Sketch of the unit cell of a soft elastic foam containing serpentine ligaments. (b) Simulated deformation and fracture process in the soft elastic foam. The shading shows the dimensionless strain energy density W/W_c. The deformed shape is plotted by downscaling the actual displacement value to 10%. 26

Figure 2.9. Calculated fracture energy of soft foam structures with serpentine ligaments, as a function of the solid volume fraction ψ. The structures have identical unit-cell size and ligament thickness. The volume fraction is controlled by changing the width of the serpentine pattern, as indicated by the insets. 27

Figure 2.10. The calculated nominal-stress-stretch curve of a soft foam with serpentine ligaments as shown by Fig. 8 (without a pre-existing crack). The initial stiffness of the structure is more than two orders of magnitude lower than the solid material. The stress-stretch curve exhibits a strain-stiffening behavior, even though the material is taken to be neo-Hookean. 28

Figure 3.1. (a) Sketch of the fabrication process of the DN composite. (b) Photograph of a test sample of DN composite gripped between acrylic glass slides. 35

Figure 3.2 (a) Force-stretch curves of a VHB tape, a fabric mesh, and the DN composite with 1 layer of mesh and 2 layers of VHB tape. For comparison, the force of the VHB tape was multiplied by 2 due to DN composite contains 2 VHB tape layers. The insets A-F are snapshots of the sample correspond to the specific points along the loading curves. Over the stress plateau (B-F), partially damaged regions coexisted with the undamaged regions, and the stretch was accompanied by the growth of the damaged regions. In the strain-hardening state (F-G), the entire sample was in a partially damaged state, and the stretch caused further sliding. (b) Comparison between the partial damage process in the DN composite and a similar mechanism in DN gels. 37

Figure 3.3. Nominal stress-stretch curves of the DN composite at various compositions, from 2:3 to 1:5. The three stages are delimited roughly by the dashed lines. 39

Figure 3.4. Loading and unloading curves for a 1:2 DN composite sample subject to uniaxial tension. 40

Figure 3.5. Snapshots of the crack propagation and damage evolution in pre-cracked samples of the DN composite, together with the results of a VHB tape. The fracture process zones are encircled by the dashed lines. The arrow points at the crack tip of the VHB tape. The first snapshots were taken under the same stretch across the three samples. The second snapshots were taken at the moments when the cracks started to propagate. The third snapshots were captured during the crack propagation. 41

Figure 3.6. (a) Force-stretch curves of pre-cracked samples of the DN composite at various compositions, compared to that of a mesh-only sample. (b) Nominal stress-stretch curves of pre-cracked samples at various compositions, compared to that of a tape-only sample. 42

Figure 3.7. Fracture work of pre-cracked samples of VHB tape and DN composite with various compositions as indicated. 44

Figure 3.8. Sketch illustrating the interaction between the mesh and the tape. The membrane force/stress distribution in the mesh and tape layers. The mesh acts like the 1st network in a DN gel, while the tape acts like the 2nd network. 45

Figure 3.9. Sketch of the stick-slip behavior due to the discrete nature of the nature, in stage II of the DN composite under uniaxial tension. 48

Figure 3.10. The peak stress and plateau stress of the DN composite, plotted as functions of the inverse of the tape thickness, $1/H$. The dots show the experimental data, and the curves show the estimation from theory. The error bars indicate the range of data. 49

Figure 3.11. Stress-stretch curves of the DN composite as predicted by the theoretical model. The five curves have the same mesh-to-tape ratios as the corresponding ones in Fig. 3.3. Detailed derivation is given in the Electronic Supplementary Information, and the material parameters are extracted from independent experiments on the base materials individually. 51

Figure 4.1. Sketch of the manufacture process of the PDMS-magnets composite..... 58

Figure 4.2. Force-Extension curves of PDMS-Magnets composite, and DN composite with single chain of magnets. The insets A–E are the snapshots of the sample corresponding to the specific points along the loading curves. Over the stress plateau (A-E), partially damaged regions coexisted with the undamaged regions, and the extension was accompanied by the growth of the "damaged" regions. In the strain-hardening state, the entire magnet chain was separate, and the extension caused further sliding between magnets and PDMS. 59

Figure 4.3. Nominal stress-strain curves of DN composite at various compositions, from volume fraction 35% to 17%. The initial region curves with an exaggerated strain scale shown at bottom left. 60

Figure 4.4. Loading and unloading curves for a DN composite sample (volume fraction 26%) subjected to uniaxial tension. 61

Figure 4.5. Dimensionless stress-strain curves of one unit cell (26% volume fraction) as predicted by the theoretical model. The material parameters are extracted from independent experiments on the base materials individually. The experimental magnets data shows in blue square. The experimental PDMS data plot in black triangle. 64

Figure 4.6. Theoretical dimensionless stress-strain curves of one DN composite (26% volume fraction) for case when 1,2,3,4 and 5 pairs of magnets are separated. The sketch of magnets chain in bottom was indicate 2 unit cells are open. 66

Figure 4.7. The peak stress of DN composite, plotted as functions of volume fraction. The dots show the experimental data. And the curve shows the estimation from theory. The error bars indicate the range of data. 67

Figure 4.8. Sketch illustrating the interaction between PDMS and magnets..... 68

Figure 4.9. Schematic sketch of actual loading and unloading curve above and under theoretical curve. 69

Figure 4.10. Nominal stress-strain curves of a VHB-Magnet composite. The insets A–Eare the snapshots of the sample corresponding to the specific points along the loading curves. Over the stress plateau (A-E), partially damaged regions coexisted with the undamaged regions, and the extension was accompanied by the growth of the "damaged" regions. In the strain-hardening state, the entire magnet chain was separate, and the extension caused further sliding between magnets and VHB tape..... 70

Figure 5.1. Loading curve of a representative DN gel (PAMPS/PAAm DN gel) under uniaxial loading case, and pictures demonstrating the necking process. The insert alphabets represent the correspondence between the pictures and the arrowed data points. 73

Figure 5.2. Loading curves of DN gel for repeated loading cycles. 74

Figure 5.3. Dilatant stress-strain behavior of the composite shows transformation toughening behavior. The right curve for $B < 0$ shows some softening effect. 76

Figure 5.4. Left: Height of transformation zone for $B < 0$ transforming materials. Right: Ratio of near-tip to remote stress intensity factor. 78

Figure 5.5. Damage function dmg for the 1st network. 79

Figure 5.6. The elastic energy density function of the DN gel under uniaxial elongation deformation λ for different damage stage. 80

Figure 5.7. The stress-stretch relation of the DN gel under uniaxial elongation stretch λ. 81

Figure 5.8. The normalized stress-stretch curves of the DN gel for numerical study. The number in the legend corresponds to the shear modulus of 2nd network. The stress is normalized by the shear modulus for the 1st network, which is 1. 81

Figure 5.9. The damage zone field for 1st network and crack field for the whole structure. Both in undeformed state and current state. 83

Figure 5.10. Left: The process zone size of fracture of DN gel. Right: The transformation zone size of transformation toughening. 84

Figure 5.11. The toughening factor, the ratio between the overall fracture energy and the intrinsic fracture energy. 85

Figure 5.12. Illustration of the difference of toughening factor between fracture of DN gel and transformation toughening. The stress-strain curves are shown for very small transformation strain on the left and large transformation strain on the right. The Blue line marks the fracture of DN gel while the red line marks the transformation toughening. 86

Figure 5.13. The relation between dimensionless fracture energy of DN gel Γ and the dimensionless hysteresis energy between the loading and unloading curve Whys..... 87

Figure 5.14. The process zone in reference state and current state for three cases, $\theta T \theta e = 0.27$, $\theta T \theta e = 4.67$ and $\theta T \theta e = 7.54$. The red line corresponds to the crack. 88

ACKNOWLEDGMENTS

I would like to thank my advisor Prof. Wei Hong for his support, encouragement and patient guidance. He taught me how to be a good researcher and use innovative ideas to solve problems. With his insight and expertise, I have been introduced to a very exciting and challenging field. Soft material is a very new area and have lots of potential of application in the future.

I would like to express my special gratitude to Prof. Ashraf Bastawros, my co-major professor, for supporting me at the last semester of my Ph.D study. He brings lots of help to our experiments and raises good questions about our research. We benefit a lot through the discussion with him.

I would also like to thank my committee members, Prof. Liang Dong, for his guidance and support throughout the time of my research in his lab.

I would also like to thank my committee members, Prof. Pranav Shrotriya and Prof. Liming Xiong, for their guidance and support throughout the course of this research. I learn a lot from their courses.

In addition, I would also like to thank my group members, friends, classmates, colleagues, the department faculty and staff for making my time at Iowa State University a wonderful experience.

Last, but certainly not least, thanks to my parents, for their great support and encouragement during my graduate study.

ABSTRACT

Soft materials and structures are very common in our daily life and industry products, but still shows great potential on many innovative applications. To make better use of them, we need a good understanding of the fracture and deformation of the materials. Starting from soft elastic foams, this paper proposes a scaling law for the fracture energy of soft elastic foam by using the analogy between the cellular structure and the network structure of rubbery polymers. To verify the scaling law, a phase-field model for the fracture processes in soft elastic structures is developed. The numerical simulations in two-dimensional foam structures of various unit-cell geometries have all achieved good agreement with the scaling law. Inspired by the toughening mechanism of double-network (DN) hydrogels, a highly stretchable soft composite and a magnetic double-network composite capable of large recoverable deformation were fabricated. Just as the DN gels, the coexistence of the partially damaged and intact regions resulted in a stable necking in the composite when subjected to uniaxial tension. The propagation of the necking zone corresponded to a plateau on the stress–stretch curve. The experimental observations serve as a good evidence of the fracture process of DN gel. Finally, a phase field model for the fracture of DN gel is proposed. The numerical results are compared with transformation toughening results since the mechanical behavior of both material shows great similarity. The process zone shows similar pattern with what we observed in DN composite experiments.

CHAPTER 1. INTRODUCTION

1.1 Soft Materials and Structures

Pierre-Gilles de Gennes, the giant guy in soft material science, concludes in his Nobel Lecture that the two major features of soft materials are complexity and flexibility. [1] There are a lot of soft material and structures that either belongs to our body or appears frequently in our daily life, such as polymers, gels, liquid crystals, colloidal grains, as well as complex multicellular organisms. Despite the popularity of soft materials and structures, most research topics about mechanics of materials are limited to hard materials in last century.

Hard materials, like metal or ceramics, are deformed by stretching molecular bonds. While soft materials can be deformed in two ways: either by change molecular configuration or through solvent migration.[2] The first mode corresponds to local rearrangement of molecules, which means the shape of the gel can be changed but the volume is conserved. For example, rubber elasticity is this kind of deformation. While the second mode is a result from the long-range migration of the small molecules. Under this condition, both shape and volume of the gel can be changed. Swelling or de-swelling belongs to this mode of deformation.

We limit the scope of this work to soft materials and structures which can maintain certain shape, and are capable of recovering at least part of deformation. Including elastomers, polymeric gels, and biological materials such muscles, tendons, cartilage and blood vessels, they share the general deformation mechanism of rubber-like elasticity with the basic molecular structure of that of the natural rubber: a cross-linked long chain polymer network. For the second mode of deformation, we did some numerical study on the swelling of gel and relevant micro fluid devices, but we will not mention is here.

1.2 Applications of Soft Materials and Structures

Most engineering soft materials which have been used into real products play the roles as seals, gaskets, adhesives and tires which provide conformation between two complex structures. On the other hand, the combined property of low stiffness and the ability to sustain large deformation have drawn researchers' and engineers' attention. Hydrogels have structural similarity to the macromolecular-based components in our body and are considered bio-compatible. These novel materials have current and emerging applications mainly in three areas:

1) Soft active sensors and actuators. Gels are known as stimuli-responsive materials, due to the advantage of having two deformation mechanism as we talk about in last section. Because of their softness, solvent concentration can be controlled by the chemistry of the swelling process through swelling or shrinking the polymer network, and a gel can deform by non-mechanical driving forces. Examples of theories include temperature-sensitiveness [3], pH sensitiveness [4], eletro-sensitiveness [5], and so on. Stimuli response gels have vast amount of potential applications such as micro actuators [6-7], micromechanical engines [8], micro-fluidic valves[9], adaptive liquid microlenses[10] and etc.

2) Liquid absorbent. Liquid absorbent is the most tradition and widest applications of gels, such as baby diapers, adult incontinence products, personal hygiene products and underground liquid retention agents for both water and oil.[11] Gels used for this purpose are also known as the superabsorbent polymers, [11] resulted from the ability to swell by absorbing liquid or water of hundreds of the weight of iteself.

3) Tissue Engineering. Soft material, for example hydrogels, have structural similarity to the macromolecular-based components in our body and are considered biocompatible. The distinct low modulus of gels comparing to all other engineering materials

allows a gel made devices to conform and deform with surrounding tissues without causing damage. Besides, cells are capable of perceiving and responding to the stiffness of the substrate it attached to.[12] Gels acts as tissue scaffolds that integrate the implant with the living environment by providing the tunable mechanical environment for cell growth.[13] There also has been considerable progress in recent years in addressing the clinical and pharmacological limitations of hydrogels for drug delivery applications.[14] Other than this, artificial cartilage[15], wound dressing as well as tissue bulking material are also popular applications of hydrogels and soft materials.

1.3 Fracture of Rubber

Fracture energy of a hard material is the energy of breaking one layer of atomic bonds to create new surface, which equals twice of the surface energy of that materials. Typical value of Γ is on the order of $1\,J/m^2$ for glass and $10\,J/m^2$ for ceramics. On the other hand, Γ of elastomers range from $10^2\,J/m^2$ to $10^5\,J/m^2$ [16-17], the higher limit of which is comparable to that of ductile metals.

Lake and Thomas [16] proposes a model that suggests the origin of the large value of is due to the loss of strain energy in the polymer chains as they rupture. Immediately prior to fracture, the polymer chain is likely to be fully extended with each monomer being comparably stretched. The elastic energy per monomer approximately equals to the bond energy, and the total energy needed to rupture the fully extended chain is the number of monomers per chain times the energy required to stretch one link to the breaking limit. Given the large amount of monomers per chain in rubber, such a mechanism explains the discrepancy between the fracture energy threshold of rubber and that of brittle crystals. After chain rupture, all the strain energy is lost due to local dissipation on the chain. Overall, the

intrinsic fracture energy consists of two parts: the intrinsic viscous dissipation, which is a dominating part, and a small value of bonding energy of a single link.

1.4 Dissertation Outline

The main point of this work focus on the fracture and deformation of soft materials and structures. Consisting of both experimental, analytical and numerical results, we investigate the fracture behavior and related mechanics problem of soft foam, two composites (one highly stretchable and one recoverable) and DN gel.

In chapter 2, we introduce the phase field model and the scaling law for fracture energy of soft elastic foam. Consisting of stretchable and flexible cell walls or ligaments, soft elastic foams exhibit extremely high fracture toughness. Using the analogy between the cellular structure and the network structure of rubbery polymers, we propose a scaling law for the fracture energy of soft elastic foam. To verify the scaling law, a phase-field model for the fracture processes in soft elastic structures is developed. The numerical simulations in two-dimensional foam structures of various unit-cell geometries have all achieved good agreement with the scaling law. In addition, the dependences of the macroscopic fracture energy on geometric parameters such as the network connectivity and spatial orientation have also been revealed by the numerical results. To further enhance the fracture toughness, a type of soft foam structures with nonstraight ligaments or folded cell walls has been proposed and its performance studied numerically. Simulations have shown that an effective fracture energy one order of magnitude higher than the base material can be reached by using the soft foam structure.

In chapter 3, a soft composite consisting of a fabric mesh and VHB tape layers was fabricated, which is inspired by the toughening mechanism of double-network (DN)

hydrogels. The composite was as stiff as the fabric mesh, and as stretchable as the VHB tape. At certain compositions, the composite was significantly stronger and tougher than the base materials. The extensibility and toughness of the composite can be attributed to a damage delocalization mechanism similar to that of the DN gels. In the partially damaged regions, the fabric mesh fragmented into small islands, surrounded by the highly stretched VHB tapes. Accommodated by the finite sliding at the interface, the large deformation of the composite is highly non-affine. Just as the DN gels, the coexistence of the partially damaged and intact regions resulted in a stable necking in the composite when subjected to uniaxial tension. The propagation of the necking zone corresponded to a plateau on the stress–stretch curve. During cyclic loading, the composite also exhibited stress hysteresis with almost recoverable strain, similar to that in a DN gel. To rationalize these observations and to better understand the underlying physical mechanism, a simple 1D model has been developed for the damage evolution process in the composite. The predictions of the model have achieved good agreement with the measured properties of the composite of various compositions. Furthermore, the composite itself may also be regarded as a macroscopic model when studying the properties and toughening mechanism of the DN gels.

Chapter 3 further develop the DN idea and extend it to a recoverable DN composite which consists of permanent magnets and a PDMS layer. The magnets were initially connected into fibers which provided the composite relatively high stiffness. Under a critical axial tension, the magnets separated from each other in sequence, and transferred the load to the elastomeric matrix. Exhibiting a long plateau over the stress-strain curve, the damage evolution process was similar to that of DN gels and elastomers. The strength of the composite was limited by the magnetic attractions while the maximum stretch was limit by

the stretchability of the matrix. The composite was significantly tougher than either of the constituents. Upon unloading, the magnetic attraction between neighboring magnetics held them back again and the composite's stiffness and strength were fully recovered. A simple 1-D model is proposed and matches the experimental results very well.

Chapter 4 finally goes back to the fracture of DN gel. A phase field model for fracture of DN gel is proposed and several numerical examples have been calculated. The stress strain relation of DN gel is compared with transformation toughening phenomenon in composite. The process zone size as well as the toughening factor are investigated. The overall fatigue fracture threshold and its scaling law is discussed. The process zone shape and the fully transformed part are compared with transformation toughening results. The experimental results also serve as an evidence for the process zone shape of DN gel in numerical studies.

1.5 References

[1] P.G. de Gennes. (1991) Nobel lecture--soft matter. On line at (https://www.nobelprize.org/uploads/2018/06/gennes-lecture.pdf)

[2] Hong, Wei, et al. "A theory of coupled diffusion and large deformation in polymeric gels." Journal of the Mechanics and Physics of Solids 56.5 (2008): 1779-1793.

[3] Otake, Katsuto, et al. "Thermal analysis of the volume phase transition with N-isopropylacrylamide gels." Macromolecules 23.1 (1990): 283-289.

[4] Marcombe, Romain, et al. "A theory of constrained swelling of a pH-sensitive hydrogel." Soft Matter 6.4 (2010): 784-793.

[5] Shiga, Tohru. "Deformation and viscoelastic behavior of polymer gels in electric fields." Neutron spin echo spectroscopy viscoelasticity rheology. Springer, Berlin, Heidelberg, 1997. 131-163.

[6] Carpi, Federico, and Elisabeth Smela, eds. Biomedical applications of electroactive polymer actuators. John Wiley & Sons, 2009.

[7] Hu, Zhibing, Xiaomin Zhang, and Yong Li. "Synthesis and application of modulated polymer gels." Science 269.5223 (1995): 525-527.

[8] Steinberg, I. Z., A. Oplatka, and A. Katchalsky. "Mechanochemical engines." Nature 210.5036 (1966): 568.

[9] Richter, Andreas, et al. "Influence of volume phase transition phenomena on the behavior of hydrogel-based valves." Sensors and Actuators B: Chemical 99.2-3 (2004): 451-458.

[10] Dong, Liang, et al. "Adaptive liquid microlenses activated by stimuli-responsive hydrogels." Nature 442.7102 (2006): 551.

[11] Buchholz, Fredric L. "Superabsorbent polymers." Encyclopedia of Polymer Science and Technology (2002).

[12] Discher, Dennis E., Paul Janmey, and Yu-li Wang. "Tissue cells feel and respond to the stiffness of their substrate." Science 310.5751 (2005): 1139-1143.

[13] Drury, Jeanie L., and David J. Mooney. "Hydrogels for tissue engineering: scaffold design variables and applications." Biomaterials 24.24 (2003): 4337-4351.

[14] Hoare, Todd R., and Daniel S. Kohane. "Hydrogels in drug delivery: Progress and challenges." Polymer 49.8 (2008): 1993-2007.

[15] Azuma, Chinatsu, et al. "Biodegradation of high-toughness double network hydrogels as potential materials for artificial cartilage." Journal of Biomedical Materials Research Part A: An Official Journal of The Society for Biomaterials, The Japanese Society for Biomaterials, and The Australian Society for Biomaterials and the Korean Society for Biomaterials 81.2 (2007): 373-380.

[16] Lake, G. J., and A. G. Thomas. "The strength of highly elastic materials." Proc. R. Soc. Lond. A 300.1460 (1967): 108-119.

[17] Gent, A. N. "A new constitutive relation for rubber." Rubber chemistry and technology 69.1 (1996): 59-61.

CHAPTER 2. PHASE FIELD MODEL AND FRACTURE OF SOFT ELASTIC FOAM

2.1 Introduction

Solid foam, a state of material characterized by the highly porous cellular structure, is commonly found in nature and in everyday life. In industrial applications, solid foams are well known for their superior energy-absorbing capability under compression [2-4]. Their fracture properties have also attracted great interests [4-9]. Scaling laws between fracture properties and porosity have been proposed and widely accepted [4,5]. However, most existing theories are based on linear elastic fracture mechanics and the cell walls of the foams are assumed to be linear elastic prior to rupture. While such theories and predictions can be applied to foams of relatively stiff materials (e.g. ceramics and metals), their applicability becomes questionable to those consisting of soft and highly stretchable materials, such as elastomers. For example, an early experimental study on polyurethane foams found the fracture energy to be less dependent on the density, and even exhibiting a slight decrease when density increases [10], while the scaling laws of rigid foams all demonstrate linear or power-law dependence of the fracture energy over density [4,5].

The major difference between stiff brittle foam and soft elastic foam lies in the porosity and the slenderness of cell walls (or ligaments for an open cell foam). For simplicity, in the following discussion, the two types of foams will be referred to as rigid foam and soft foam, respectively. In contrast to the cell walls of rigid foam which partially shares the load after rupture, a fractured cell wall of soft foam merely dangles over the rest of the structure. Such a structural difference induces the dramatic distinction in energy transmission during fracture. Upon rupture, the remaining elastic energy in a cell wall of

rigid foam could be redistributed according to the crack-tip advancement, while that in a slender component could hardly be transferred to its neighbors. The elastic energy in a ruptured slender component is mostly dissipated through local vibration or viscoelastic deformation. As a result, the effective fracture energy would have to include the energy of the entire component rather than just that at the vicinity of the crack faces (i.e. the surface energy).

To better understand this unique mechanism of toughening, one may consider the fracture process of a rubber, in which the crosslinked network of long polymer chains could be regarded as an extreme case of soft foam when each slender ligament shrinks down to a molecular scale. In their classic paper, Lake and Thomas suggest the fracture mechanism of rubber fracture: the energy needed to rupture a polymer chain is much larger than that of a single bond as the entire chain is subject to virtually the same breaking force [11]. After fracture, the broken chains recoil and their entropic elastic energy would not be forwarded to neighboring chains. Thus, the intrinsic fracture energy of rubber scales approximately as $\Gamma_{\text{rubber}} \sim Nn^{\frac{3}{2}} l_{\text{m}} U$, with N being the number of chains per unit volume, n the number of monomers per chain, l_{m} the length of each monomer, and U the energy needed to rupture each monomer [11]. This model has been widely used on rubber, but has seldom been related to the fracture of soft foam. Just by using the analogy, we may also deduce the scaling relation for the fracture energy of soft foam as

$$\Gamma \approx \alpha W_c \psi l \tag{2.1}$$

Here, we use W_c to represent the critical energy density of cell wall at rupture, ψ for the volume fraction (i.e. the relative density) of the solid phase, and l for the characteristic size of the foam (e.g. the height of a cell wall). α is a dimensionless geometric factor. One may

arrive at the same result from a different perspective. Due to the special geometry of foam, the sharpness of a crack is always limited by l. The fracture energy is thus given by $\Gamma \sim Wl$ [12], with $W = \psi W_c$ being the effective strain energy density at the crack tip. In the limiting case when the material is stiff enough and the fracture process can be modeled by linear elastic fracture mechanics, by using the effective modulus of the structure $E_{\text{eff}} \sim \psi^2$, this scaling law (2.1) reduces to the model of stiff foams with the fracture toughness given by $K_{\text{IC}} \sim \sqrt{\Gamma E_{\text{eff}}} \sim \psi^{\frac{3}{2}} \sqrt{l}$ (for open cells) [4]. However, the applicability of the latter, which was derived from linear elastic fracture mechanics by assuming a square-root singularity in the stress field [4], to soft elastic foams undergoing large deformation remains unknown.

It is noteworthy that due to the presence of defects, the rupture strength and thus W_c is usually size dependent, unless the cell walls are thinner than the critical size for theoretical strength. The energy-dissipation mechanism of the soft foam structure, on the other hand, is never limited to microscopic scale. One may refer to a two dimensional macroscopic analogy of soft foam, a net or a netted structure (e.g. a string bag), commonly known for its toughness and notch insensitiveness.

Even though the scaling law (1) seems natural and plausible, it could be hard to verify it directly through experiments. In practice, it is difficult to control the porosity and cell size independently during polymer processing, not to mention the size dependency of W_c. Alternatively, this paper seeks to verify the scaling law through numerical modeling. In the following sections, a phase-field model for rubber fracture will be adopted to simulate the damage initiation and evolution in hyperelastic cellular structures. The phase-field model for fracture, which is capable of calculating the crack growth according to the energy criterion without a predetermined crack path, is very suitable for structures with complex geometries

such as soft elastic foams. The scaling law and the special toughening mechanism will then be demonstrated with the phase-field model. The dependence on the detailed geometry of the foam cells will also be studied.

2.2 Phase-field model of fracture

Numerical simulation of fracture processes has the inherited difficulties in dealing with discontinuities, singularities, and moving boundaries which causes large geometric and even topologic changes. To overcome some of these difficulties, phase-field models of brittle fracture have been developed [1, 13-18, 22]. Recently, phase-field models have also been applied to the brittle fracture of rubbery polymers [23]. Numerical experiments have already shown that these models are capable of capturing both the onset of crack propagation and the damage morphologies of dynamic cracks [19-21]. Without the need to track individual crack or to prescribe a crack path, the phase field method becomes a promising candidate for modeling the fracture of structures with relatively complex geometries, such as the soft elastic foam. The model used in this paper closely follows these developments, especially those by Karma et al [13] and Hakim and Karma [14].

To describe the state of material damage and to avoid tracking the crack front and faces, a phase field $\phi(\mathbf{X},t)$ varying continuously between the intact region ($\phi=1$) and a fully damaged region ($\phi=0$) is introduced. The loss of integrity in the solid is modeled by writing the elastic strain energy density as a monotonic increasing function of the damage variable, $g(\phi)W_s^0(\mathbf{F})$, where W_s^0 is the strain-energy density of the intact material under the same strain, and g is an interpolation function in the interval $(0,1)$ with vanishing derivatives on both ends. In this study, we choose the interpolant $g(\phi)=4\phi^3-3\phi^4$. As a common

practice of hyperelasticity, the deformation gradient tensor $\mathbf{F}$ is used to represent the state of strain. Following Karma et al. [13], we write the free energy density function to include three contributing terms:

$$W(\phi,\nabla\phi,\mathbf{F}) = g(\phi)W_s^0(\mathbf{F}) + [1-g(\phi)]W_c + \frac{\kappa}{2}|\nabla\phi|^2 . \tag{2.2}$$

The second term on the right hand side of Eq. (2.2) represents the energy associated with material damage. When the strain energy at a material particle exceeds the threshold W_c, the damaged state with $\phi = 0$ becomes energetically favorable. Just as in almost all phase-field models, the gradient energy term is added to regulate a smooth transition between the coexisting states. In this paper, the material constituting the solid phase of the foam is assumed to be isotropic, so that only a scalar coefficient κ is needed for the gradient energy term. In equilibrium, the combination of the second and third terms on the right hand side of Eq. (2.2) gives the surface energy, i.e. half of the intrinsic fracture energy. The fracture energy of the material modeled by the energy function is approximately $\Gamma \approx 2\sqrt{\kappa W_c}$ [13]. Here, in a body undergoing finite deformation, all energy densities are measured with respect to the volume in the reference state.

Countless number of constitutive models have been developed for hyperelastic solids. Although specific stress-strain relations of the solid phase may affect the ultimate fracture properties of soft foam, such dependence is beyond the scope of the current paper. Here for simplicity, we will limit the discussion to a neo-Hookean material of the strain energy function

$$W_s^0(\mathbf{F}) = \frac{\mu}{2}(\mathbf{F}:\mathbf{F}-3), \tag{2.3}$$

where μ is the initial shear modulus. In contrast to linear elastic solids, rubbery polymers are often modelled as incompressible. To enforce volume incompressibility, approaches such as the application of the Lagrange multiplier are often taken, e.g. by adding to the free energy function a term $-p(\det\mathbf{F}-1)$ with a Lagrange multiplier p representing the pressure field. A physically meaningful model needs to degrade the compressibility simultaneously with the shear stiffness. Directly multiplying the Lagrange multiplier term by $g(\phi)$ obviously does not serve the purpose. Instead, we modify the Lagrange multiplier term slightly by modeling the material as slightly compressible:

$$-pg(\phi)(\det\mathbf{F}-1)-\frac{1}{2}\frac{p^2}{K}. \tag{2.4}$$

By taking the variation of (2.4) with respect to p, one will arrive at an equation of state with a degrading bulk modulus: $p=-g(\phi)K(\det\mathbf{F}-1)$. In the intact state, the large bulk modulus $K>>\mu$ ensures volume conservation; in the fully damaged state, the added term does not affect the field of deformation, and the ad-hoc field p is regulated numerically by the quadratic term in (2.4).

With all the aforementioned energy contributions, the total free energy of the system is simply the volume integral of the energy density, including the terms in (4), and the surface integral of the potential of external tractions $\mathbf{t}$:

$$\Pi[\phi,\mathbf{x}]=\int W dV-\int \mathbf{t}\cdot\mathbf{x}dA, \tag{2.5}$$

where $\mathbf{x}(\mathbf{X},t)$ symbolizes the current coordinates of a material particle located at $\mathbf{X}$ in the reference state. The total free energy Π is a functional of the field of damage $\phi(\mathbf{X},t)$ and the field of deformation characterized by $\mathbf{x}(\mathbf{X},t)$. Following Hakim and Karma [14], we

neglect inertia and body forces, and assume the system to be in partial mechanical equilibrium, so that $\delta\Pi/\delta\mathbf{x} = \mathbf{0}$ or

$$\nabla \cdot \mathbf{s} = \mathbf{0}, \tag{2.6}$$

in the bulk, and $\mathbf{N} \cdot \mathbf{s} = \mathbf{t}$ on the surfaces. Here $\mathbf{s} = \partial W/\partial \mathbf{F}$ is the nominal stress, and $\mathbf{N}$ is the unit normal vector on a surface. For the evolution of the phase field ϕ, on the other hand, we assume a linear kinetic law with isotropic mobility m:

$$\dot{\phi} = -m\frac{\delta\Pi}{\delta\phi} = m\left[\kappa\nabla^2\phi - g'(\phi)\left(W_s^0 + p\det\mathbf{F} - W_c\right)\right]. \tag{2.7}$$

To simulate quasi-static fracture processes, a large enough mobility is taken to achieve rate-independent results. Further, to model the irreversibility of fracture processes and to prevent the damaged phase from healing, we force ϕ to be a monotonically decreasing function of time by taking only the positive part of the driving force [22]:

$$\dot{\phi} = -m\left\langle g'(\phi)\left(W_s^0 + p\det\mathbf{F} - W_c\right) - \kappa\nabla^2\phi\right\rangle, \tag{2.8}$$

where the angular brackets indicate an operation of taking the positive values, $\langle\xi\rangle = \left(\xi + |\xi|\right)/2$. Supplemented by proper initial and boundary conditions, Eqs. (2.6) and (2.8) constitute a partial differential system for the coevolution of deformation and damage fields, $\mathbf{x}(\mathbf{X},t)$ and $\phi(\mathbf{X},t)$.

2.3 Energy dissipation and numerical implementation

The major difference between soft and stiff foams and the primary means of energy dissipation during fracture can be qualitatively understood with the aid of Fig. 2.1. For ease of description, we will refer to the solid dividing segments in both open and closed foams as

ligaments from now on. Upon rupture from stretched states, a ligament will first be accelerated by its own retracting forces, and the elastic energy stored prior to rupture is mostly converted to kinetic energy. When the ligament retracts further, the difference between stiff and soft ligaments is revealed: while a stiff ligament will remain straight and decelerate and transfer the energy further to the neighboring components, a soft ligament will tend to buckle or coil due to its slenderness, and the energy could not be effectively transferred. The ultimate factor is the stiffness ratio between the surrounding structure and the broken ligament (a buckled ligament has very low stiffness), as elastic wave cannot propagate from a compliant medium to a rigid one. As a result, the elastic energy of a soft ligament is mostly damped through subsequent vibration of itself.

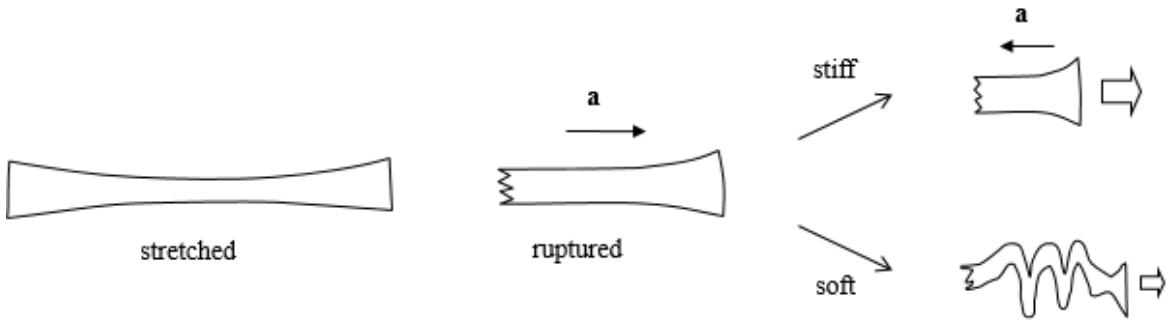

Figure 2.1. *The rupture and retraction process of a ligament (or cell wall) in a foam structure. Because of its slenderness, a soft filament will tend to buckle or coil and could not effectively transduce energy.*

The detailed process and the dependence on the structural geometry, such as the aspect ratio of each ligament and the spatial connectivity at each node, can be simulated by computing the full dynamic response of a ligament and the surrounding structure. Such analysis, however, is not of particular interest to the current paper. We will focus on soft foams with very slender ligaments, and hypothesis that most part of the elastic energy stored

in the broken ligaments will be dissipated through this process. The results are thus inapplicable to relatively stiff foams. On the other hand, it is also computationally less feasible to model the full dynamic behavior of each ligament in a foam structure of complex geometry. Instead, we will neglect the inertia and model the fracture process as quasi-static. In this limit, the dissipation through crack propagation is negligible, and the fracture energy is mainly dissipated through viscosity. Without considering dynamics, the snap back of the ligaments are fully damped after each rupture event. Instead of a proof or evidence, the calculations presented as follows are the consequence of the proposed energy-dissipation mechanism.

Similar as in many other methods for fracture and damage simulation (e.g. cohesive element and element deletion), without inertia, the damage-induced softening is intrinsically unstable. To stabilize numerical procedures, and more importantly to dissipate the redundant strain energy in the dangling ligaments after rupture, we introduce a Newtonian-fluid-like damping term to the nominal stress

$$\mathbf{s} = \frac{\partial W}{\partial \mathbf{F}} + \frac{\eta}{2}\nabla \dot{\mathbf{x}} \tag{2.9}$$

with η being the numerical viscosity. For relatively small viscosity η, the viscous stress only has significant contribution at the regions of high deformation rate, which is expected to occur only in a retracting ligament upon rupture. Numerical experiments have shown that when a small value of η is taken, the artificial viscosity only changes the rate of structural unloading at the wake of a propagating crack, and does not affect the energy consumption.

Substituting Eq. (2.9) into (2.6), one may obtain the coevolution of deformation and damage fields by solving the partial differential system (2.6) and (2.8) simultaneously. The

system has an intrinsic length scale, $r = \sqrt{\kappa/W_c}$, which is approximately the thickness of the transition zone from the intact region to a full damaged region. It could be argued that r physically characterizes the width of the fracture process zone in the condensed solid phase. Without losing generality, we rewrite the governing equations into a dimensionless form by normalizing all energy densities and stresses by W_c, all lengths by r, and time by $1/mW_c$. After normalization, the dimensionless fracture energy of the solid phase is approximately 2, and the system has only three dimensionless parameters: the normalized shear modulus μ/W_c, bulk modulus K/W_c, and viscosity $m\eta$. In the following numerical examples, we will take dimensionless modulus $\mu/W_c = 0.2$, which corresponds to the representative values of a soft elastomer: $\mu \sim 10\,\text{MPa}$, $r \sim 1\,\mu\text{m}$, and $\Gamma \sim 50\,\text{N/m}$. The dimensionless bulk modulus is taken to be $K/W_c = 200$, and the viscosity $m\eta = 10^{-4}$. It should also be noted that the ligament thicknesses of most structures calculated in the current paper are comparable to the intrinsic length scale r. In this limit, the calculations could as well be done by using the regular strength-based material degradation approach. Here, the phase-field approach is taken so that the direct comparison with the fracture process of a bulk material with the same property could be made when needed.

The dimensionless equations are implemented into a finite-element code through the commercial software COMSOL Multiphysics 4.3b. For numerical robustness under large deformation, the geometries are discretized by using triangular elements, and both the displacement and damage fields are interpolated with linear Lagrange shape functions. To capture the transition at the interface between the damaged and intact phases, a maximum mesh size of $0.5r$ is prescribed. The model is integrated over time via a fully coupled

implicit scheme, with adaptive step size. To numerically enable damage nucleation, spatial random distributions of the initial shear modulus and the intrinsic fracture energy has been introduced to each model, with standard deviation at 1% of the corresponding magnitudes.

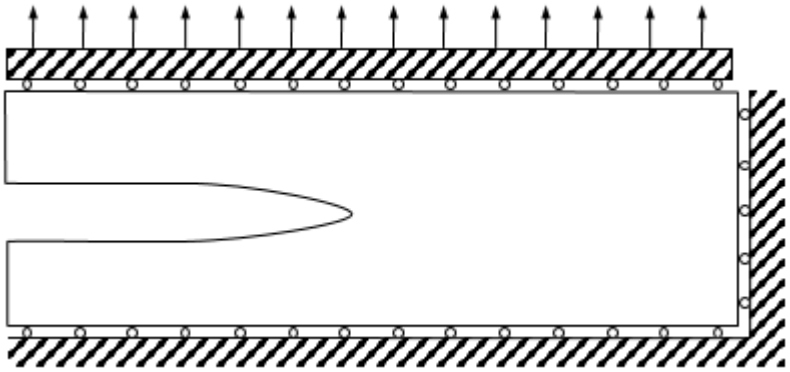

Figure 2.2. *Sketch of the loading conditions for the foam structures*

To compute the fracture energy, we load the pre-cracked structures in a similar way as the pure-shear test for rubber. As sketched in Fig. 2.2, the right and bottom edges are constrained by rollers, and the top edge is loaded by a uniform displacement. For symmetric structures and if the crack propagates along a symmetry line, only half of the structure is calculated and a symmetry boundary condition is prescribed along the symmetry line. A ramping displacement load is applied within a short time and then held constant. The crack will start to propagate when the applied displacement exceeds certain value. In a steady state when the crack tip is far from either ends, the energy release rate is independent of the crack length,

$$G = W_{\text{eff}} H \,, \tag{2.10}$$

where H is the undeformed height of the structure. W_{eff} is the effective strain-energy density in the absence of the crack, and is averaged over the volume including the space of

the pores. In contrast to the standard pure-shear test, the entire structure is under plane-strain condition, and is allowed to shrink horizontally. The corresponding 2D results are closer to the behavior of 3D closed foam. Although the effective strain-energy density W_{eff} can be calculated by integrating W at the region far ahead of the crack tip, here we calculate it separately by subjecting a non-cracked structure to plane-strain uniaxial tension.

2.4 Results and discussion

The simulations are first carried out on hexagonal (honeycomb) structures, as shown schematically in Fig. 2.3a.

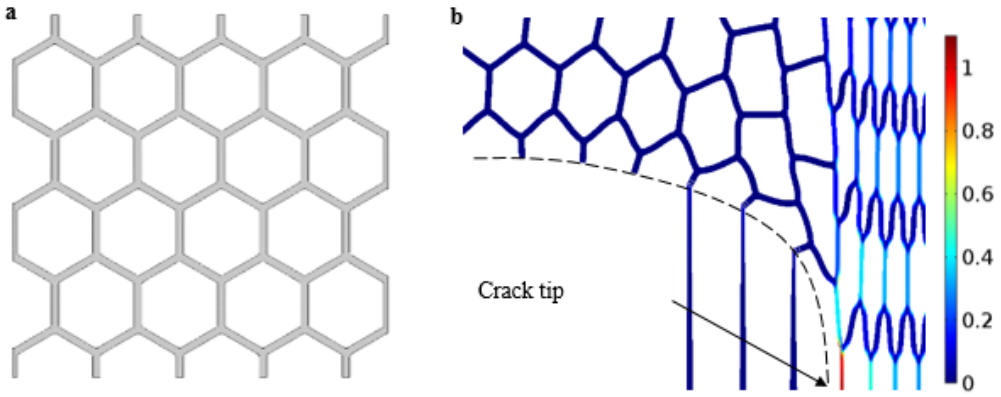

Figure 2.3. *(a) Part of the 2D honeycomb foam structure being simulated. (b) The calculated deformation and damage fields of a honeycomb structure, during the propagation of a preexsting crack. The shades represent the dimensionless strain energy density W/W_c. The crack profile is indicated schematically by the dash line, which goes through the the transition zone from the intact to the fully damaged regions in terms of ϕ. The deformation is shown to scale, and only part of the structure near the crack tip is shown. The actual computational domain is much larger than that shown to circumvent size-effect.*

In order to reduce boundary effect, the actual computational domain is much larger than that shown. Fillets of dimensionless radius 1 have been applied to all corners to reduce stress concentration, as the preferential damage of the triple junctions may result in a

different scaling law. The local deformation and damage fields of a representative result are shown in Fig. 2.3b, in which the preexisting crack has propagated through three ligaments.

In a steady state, a crack is propagating through the structure at a constant speed, the energy release rate G is given by Eq. (2.10). However, due to the discrete nature of the structure, the crack propagation appears staggered.

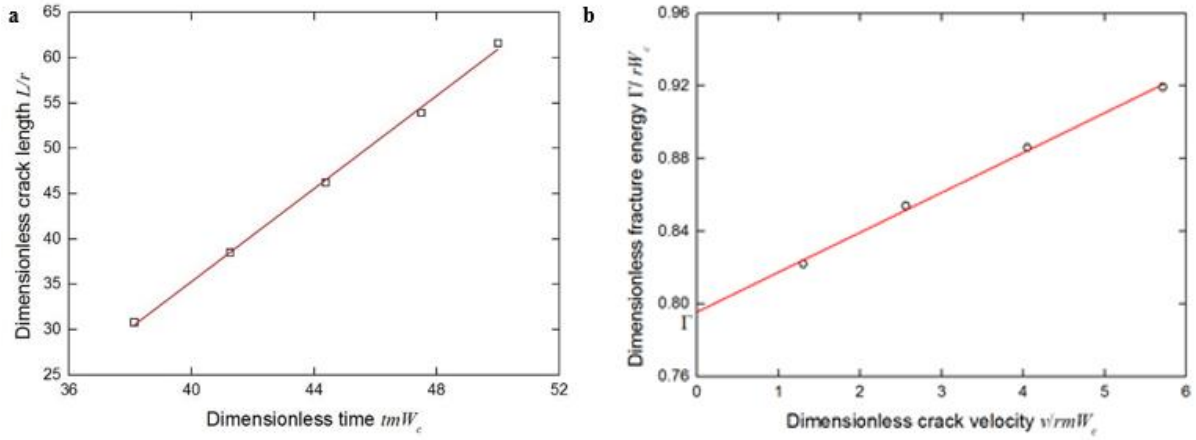

Figure 2.4. *(a) Undeformed coordinates of the ligaments as a function of the times of rupture. The line is the best linear fit. The slope indicates the dimensionless crack velocity. (b) Dimensionless fracture energy (energy-release rate)* Γ/rW_c *as a function of the dimensionless crack velocity* v/rmW_c. *The line is the best linear fit, and the vertical intercept shows the quasi-static fracture energy of the soft foam.*

To capture the effective crack velocity, we identify each event of ligament rupture, and record the time of the event and the horizontal coordinate of the corresponding ligament in the undeformed state, as shown by Fig. 2.4a. It is found that when the crack front is far from the edge, the ligament-rupture events are almost equally distributed in time, indicating a steady-state crack propagation. The slope of the linear fit to the rupture events under each loading condition is taken to be the nominal crack velocity v. In consequence of the kinetic law, Eq. (2.7) or (2.8), the energy release rate G, i.e. the driving force of the crack, is rate

dependent. As shown by Fig. 2.4b, the effective fracture energy of the structure is a monotonic increasing function of the crack velocity. Here, to compare between different structures, we use the threshold value Γ calculated from the vertical intercept of the fracture-energy-velocity curve, as shown by Fig. 2.4b. The threshold corresponds to the fracture energy of a crack propagating quasi-statically at zero velocity. Following such a procedure, we compute the quasi-static fracture energy of various foam structures, presented as follows.

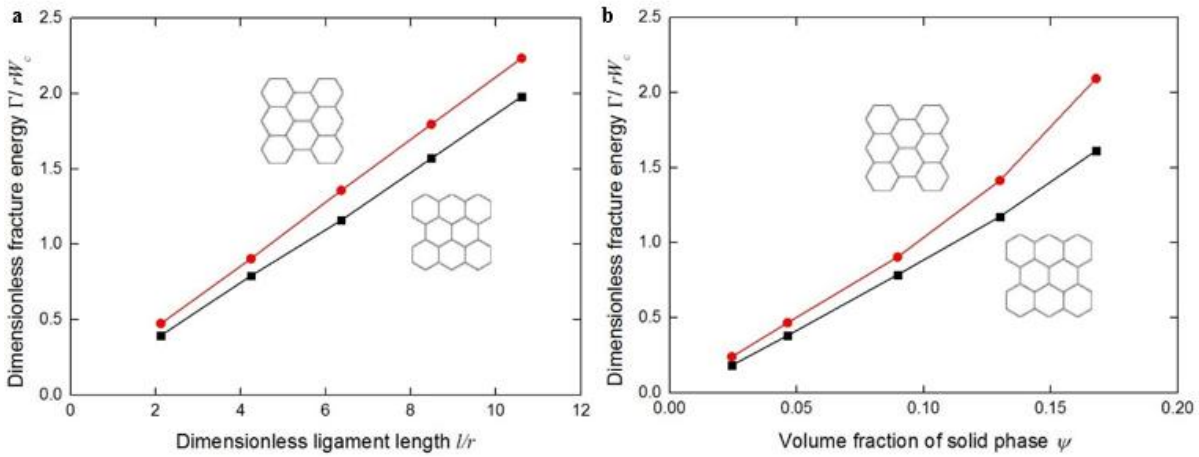

Figure 2.5. *Calculated fracture energy of the hexagonal soft foams versus (a) the normalized ligament length l/r at constant volume fraction $\psi = 9\%$, and (b) the volume fraction of the solid phase ψ at constant ligament length $l/r = 4.2$. Two different orientations are simulated as indicated by the insets (with horizontal cracks).*

The scaling relation (2.1) is verified first through the simulation on the fracture processes of hexagonal soft foams. A set of two-dimensional hexagonal foams of the same volume fraction $\psi = 0.09$ but different ligament lengths are modelled, and their quasi-static fracture energies are computed via the same procedure as described above. The resulting fracture energies of two different orientations are plotted against the ligament length in Fig. 2.5a. In both cases, the dimensionless fracture energy Γ/rW_c is approximately linear in the

ligament length l/r. Similarly, we fix the length of each ligament at $l/r = 4.2$, and vary the solid volume fraction from $\psi = 0.025$ to $\psi = 0.17$. The resulting fracture energies of the two orientations are plotted as functions of the solid volume fraction in Fig. 2.5b. As expected, at relatively small volume fraction, the fracture energy is approximately proportional to the volume fraction ψ.

Comparing between the two orientations, it is found that the fracture energy in an "armchair" orientation is consistently higher than that of the same structure in a "zigzag" orientation. Such a difference could be attributed to the anisotropy in ligament density. As illustrated by Fig. 2.6, a horizontal crack mainly goes through the inclined ligaments in the "armchair" orientation, while a crack through a foam in the "zigzag" orientation mainly breaks the vertical ligaments. The numbers of ligaments cut by unit crack length in the two orientations differ by a factor of $2/\sqrt{3}$, which explains the difference in the effective fracture energies. The same phenomena may also be understood by considering the effective sharpness of a crack. As shown by Fig. 2.6, the crack path in a "zigzag" orientation is nearly straight, while that in an "armchair" orientation is often meandering. With the crack front randomly selects one of two inclined ligaments, which has almost identical strain energies, the effective crack tip can be regarded as encompassing the region of both ligaments, and thus the crack is blunter.

The simulations on the crack propagation processes in soft foam structures of various geometries, including those with triangular and square unit cells at different orientations, all exhibit the similar linearity as that observed in the honeycomb foam, which further supports the scaling relation (2.1). The effect of unit-cell geometry is only reflected in the dimensionless coefficient α, as summarized by Fig. 2.7. Although the relatively high

fracture energy of the square-cell foam with vertical/horizontal ligaments may be explained by the higher ligament density than that of the hexagonal foam (one ligament per crack length l versus one ligament per $\sqrt{3}l$ or $2l$), the foams of other patterns do not follow the same trend. Despite the higher ligament densities, the effective fracture energies of the triangular foam or the rotated square foam are actually lower.

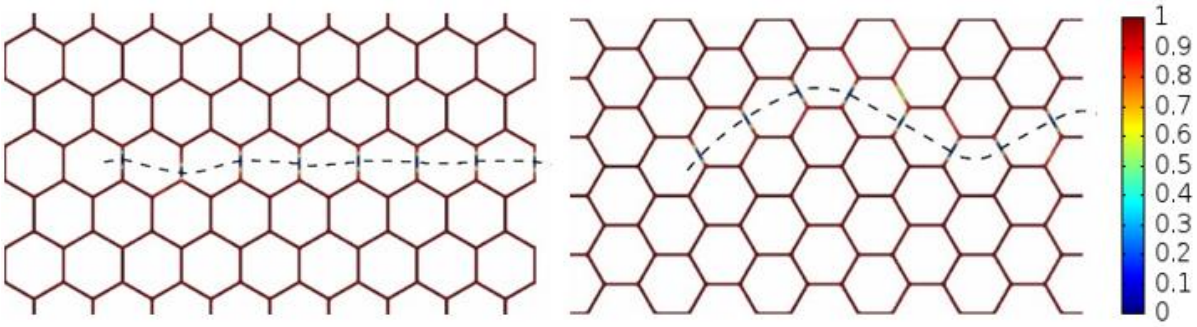

Figure 2.6. *Damage patterns of hexagonal soft foams in (a) "zigzag" and (b) "armchair" orientations. The color scale represents the damage variable ϕ, plotted in the undeformed geometry. The dash curves show the approximate paths of crack propagation.*

To understand the relatively low fracture energies, let us revisit the physical origin of the polymer-network-like toughening mechanism. Two necessary conditions must be met for the mechanism to be effective: (a) the ligaments must be relatively long and uniform, so that the elastic strain energy everywhere along a ligament is close to critical prior to rupture; (b) the network structure must be sufficiently compliant, so that the remaining strain energy after rupture is not passed to the neighboring ligaments. Even with the same aspect ratio and uniformity in the ligaments, the network connectivity in either the triangular foam or the square-cell foam is higher than that in the hexagon foam. Each node is connected to six ligaments in a triangular foam, and four in a square-cell foam, but only three ligaments are connected to each node in a hexagonal foam. Therefore, at the tip of a propagating crack in a

triangular foam of square-cell foam, two or more ligaments connected to the same node will be stretched and almost aligned in the direction perpendicular to the crack. Once one of them ruptures, the remaining elastic strain energy may be partially transferred through the common node to the other ligaments which are still standing and carrying the load along the same direction. The strain energy carried over may contribute to the further propagation of the crack, and the overall fracture energy is thus lower. It should be noted that the square-cell foam with vertical and horizontal ligaments represents a special case, in which the two lateral ligaments are connected at the direction almost perpendicular to the load, and thus the macroscopic fracture energy is less affected by the relatively high connectivity.

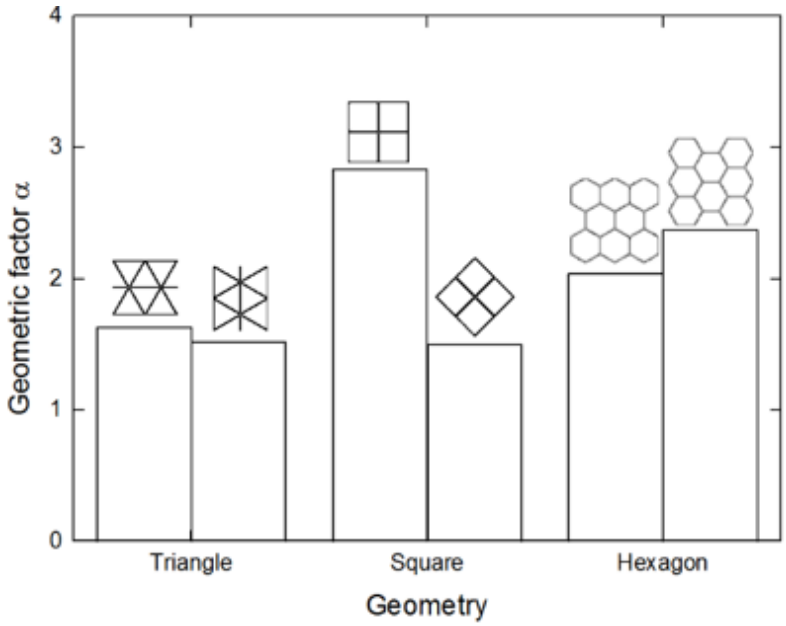

Figure 2.7. *Geometric effect on the fracture energy of soft foams. The geometries and orientations are represented by the sketch insets, with cracks running horizontally.*

Despite the apparent linear relation between the effective fracture energy and the solid volume fraction ψ (or the ligament length l), the polymer-network-like toughening mechanism is unlikely to make a soft cellular material with macroscopic pores tougher than

the bulk solid. By using the same method on a bulk solid, we have confirmed that the dimensionless fracture energy of a condensed structure is approximately 2, just as shown in the literature [23]. The factor which has not been taken into consideration here is the size-dependency of material strength. It is well-known that, due to the presence of defects, larger samples of the same material would exhibit a lower tensile strength. The critical energy density W_c which scales with the squared of the rupture strength, is dependent on the ligament thickness d (and is usually a decreasing function). On the other hand, without resolving microscopic defects, the phase-field model used in the current paper will not predict any size effect, and W_c is taken as a material parameter for normalization. Instead, if we assume the scaling relation of brittle solids from linear elastic fracture mechanics $W_c \sim d^{-2n}$ with the scaling index $n = 1/2$ [25], and follow the geometric relation for regular closed-cell foams $d \sim \psi l$, we will arrive at an effective fracture energy almost independent of ψ or l. For non-brittle materials, the scaling index n is usually less than $1/2$, and the effective fracture energy will be weakly dependent on ψ and l. Furthermore, in the limiting case when the ligaments are thin enough that the theoretical strength could be achieved, W_c will become size-independent, and the scaling law (2.1) could be fully recovered. The size-dependency of tensile strength, which has been extensively studied [24], is not a main focus of the current paper.

Here we further investigate geometric effects by studying soft elastic foams with non-straight ligaments. The scaling relation, $d \sim \psi l$, represents the geometry of closed-cell foams with relatively straight ligaments (or flat cell walls). In general, if one allows non-straight or folded ligaments, the volume fraction ψ can be varied independently from the

ligament thickness d. In other words, one may increase the solid volume fraction ψ while keeping the ligament thickness small to achieve higher fracture toughness in the structure.

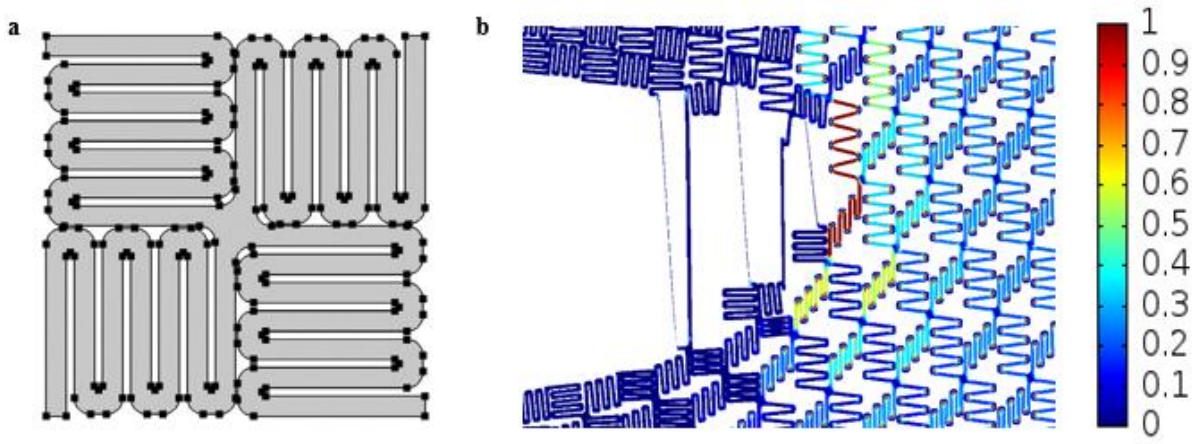

Figure 2.8. *(a) Sketch of the unit cell of a soft elastic foam containing serpentine ligaments. (b) Simulated deformation and fracture process in the soft elastic foam. The shading shows the dimensionless strain energy density W/W_c. The deformed shape is plotted by downscaling the actual displacement value to 10%.*

As an illustrative example, we construct a numerical model by repeating the unit cell as sketched in Fig. 2.8 (a). Unlike in the above examples, the initial geometry of a ligament takes a serpentine form. The material is taken to be soft enough so that the ligaments are insensitive to the stress concentration at the folding corners. During deformation, the ligaments will first be straightened and then rupture. As shown by Fig. 2.8b, the strain-energy distribution in the ligaments at the crack tip is still close to uniform, with the value close to W_c prior to rupture. By varying the width of the serpentine pattern and using the same method as in previous examples, we evaluate the fracture energy of several structures with ligament thickness taken to be r and the unit cell size $18.8r \times 18.8r$, and plot it as a function of the solid volume fraction. As shown by Fig. 2.9., the scaling law (2.1) still holds for the foam structures with serpentine ligaments. Despite the different geometries of the

unit cells, the extrapolation of the curve to lower volume fractions will give similar fracture energy levels as structures with straight ligaments. However, due to the much more condensed nature of the folding structures, the fracture energy is significantly improved. For the structure shown by Fig. 2.8, the volume fraction reaches $\psi \approx 75\%$, and the dimensionless fracture energy is $\Gamma / rW_c \approx 25$, more than one order of magnitude higher than the foam structures with straight ligaments or the same material in a bulk form.

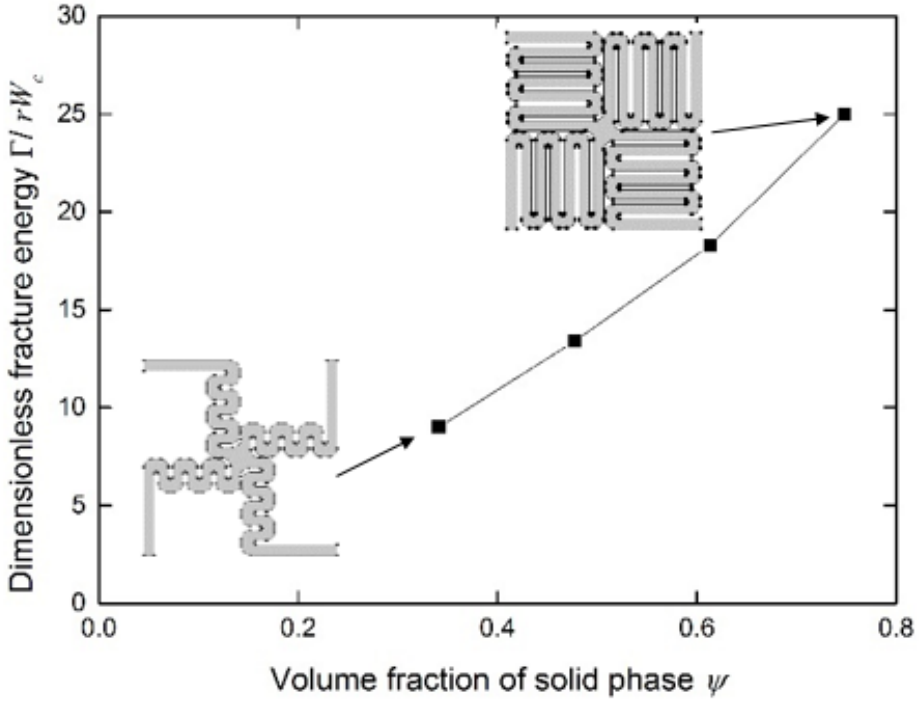

Figure 2.9. *Calculated fracture energy of soft foam structures with serpentine ligaments, as a function of the solid volume fraction ψ. The structures have identical unit-cell size and ligament thickness. The volume fraction is controlled by changing the width of the serpentine pattern, as indicated by the insets.*

Without realistic material models or optimized design parameters, this numerical example is just an illustration of the toughening mechanism. Nevertheless, it is evident that the fracture energy of a material may be significantly increased by adopting similar structural

designs. More interestingly, such a toughening mechanism is not just limited to soft solids, especially when the ligament size is small. It should also be noted that the fracture energy increase is obtained at the expense of the initial structural stiffness. As shown by Fig. 2.10., the effective initial modulus is more than two orders of magnitude lower than that of the constituting solid. Such a relation between structural compliance and fracture toughness is similar to that in the microcrack-toughening mechanism, although the latter is usually studied in the context of linear elastic fracture mechanics [26-28].

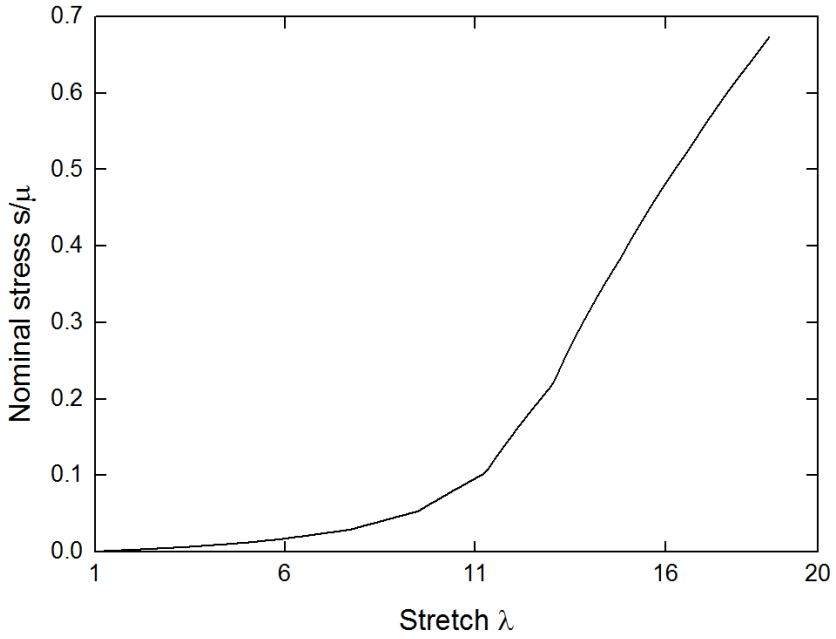

Figure 2.10. *The calculated nominal-stress-stretch curve of a soft foam with serpentine ligaments as shown by Fig. 8 (without a pre-existing crack). The initial stiffness of the structure is more than two orders of magnitude lower than the solid material. The stress-stretch curve exhibits a strain-stiffening behavior, even though the material is taken to be neo-Hookean.*

Moreover, even though the material is taken to be neo-Hookean, the stress-stretch curve exhibit a clear strain-stiffening segment at relatively large stretch, just like the behavior of elastomers at the stretch limit of polymer chains. Here, the strain stiffening corresponds to

the straightening of the serpentine ligaments. To some extent, such a structure can be regarded as a macroscopic model system for the fracture of elastomers.

The detailed design and optimization of structures of the kind, although interesting, is beyond the scope of the current paper. We are eagerly awaiting the designs and manufacturing of tough materials by utilizing this mechanism.

2.5 Conclusion

Drawing an analogy between the compliant ligaments in a soft elastic foam and the polymer chains in an elastomer, this paper proposes a polymer-network-like toughening mechanism and derives the scaling relation between the macroscopic fracture energy and the structural characteristics of soft foam structures. Different from the energy absorbing mechanism of rigid foams which is mainly effective at compression, the polymer-network-like toughening mechanism allows a soft foam to effectively dissipate energy when the structure is subject to tension. Through a phase-field model developed specifically for the fracture of elastomers, the toughening mechanism as well as the scaling relation is then verified on soft foam structures of various geometries. In addition to the scaling law, it is found that the geometric parameters such as the ligament density and the network connectivity will also affect the fracture energy of soft foams. Finally, to increase the volume fraction of the solid phase without affecting the thickness or slenderness of each ligament, a type of soft foam structures of serpentine ligaments is proposed. Numerical study suggests that such structures may reach an effective fracture energy much higher than that of the corresponding bulk material. In other words, one may toughen a soft material just by cutting slots or holes in it.

2.6 References

[1] Aranson, I. S., V. A. Kalatsky, and V. M. Vinokur. "Continuum field description of crack propagation." Physical review letters 85.1 (2000): 118.

[2] Maiti, S. K., L. J. Gibson, and M. F. Ashby. "Deformation and energy absorption diagrams for cellular solids." Acta metallurgica 32.11 (1984): 1963-1975.

[3] Han, Fusheng, Zhengang Zhu, and Junchang Gao. "Compressive deformation and energy absorbing characteristic of foamed aluminum." Metallurgical and Materials Transactions A 29.10 (1998): 2497-2502.

[4] Gibson, Lorna J., and Michael F. Ashby. Cellular solids: structure and properties. Cambridge university press, 1999.

[5] Maiti, S. K., M. F. Ashby, and L. J. Gibson. "Fracture toughness of brittle cellular solids." Scripta Metallurgica 18.3 (1984): 213-217.

[6] Gibson, L. J., et al. "Failure surfaces for cellular materials under multiaxial loads—I. Modelling." International Journal of Mechanical Sciences 31.9 (1989): 635-663.

[7] Brezny, Rasto, and David J. Green. "Factors controlling the fracture resistance of brittle cellular materials." Journal of the American Ceramic Society 74.5 (1991): 1061-1065.

[8] Chen, J. Y., Y. Huang, and M. Ortiz. "Fracture analysis of cellular materials: a strain gradient model." Journal of the Mechanics and Physics of Solids 46.5 (1998): 789-828.

[9] Bažant, Zdeněk P., et al. "Size effect and asymptotic matching analysis of fracture of closed-cell polymeric foam." International journal of solids and structures 40.25 (2003): 7197-7217.

[10] McIntyre, A., and G. E. Anderton. "Fracture properties of a rigid polyurethane foam over a range of densities." Polymer 20.2 (1979): 247-253.

[11] Lake, G. J., and A. G. Thomas. "The strength of highly elastic materials." Proc. R. Soc. Lond. A 300.1460 (1967): 108-119.

[12] Thomas, A. G. "Rupture of rubber. II. The strain concentration at an incision." Journal of Polymer science 18.88 (1955): 177-188.

[13] Karma, Alain, David A. Kessler, and Herbert Levine. "Phase-field model of mode III dynamic fracture." Physical Review Letters 87.4 (2001): 045501.

[14] Hakim, Vincent, and Alain Karma. "Laws of crack motion and phase-field models of fracture." Journal of the Mechanics and Physics of Solids 57.2 (2009): 342-368.

[15] Eastgate, L. O., et al. "Fracture in mode I using a conserved phase-field model." Physical review E 65.3 (2002): 036117.

[16] Wang, Yu U., Yongmei M. Jin, and Armen G. Khachaturyan. "Phase field microelasticity theory and modeling of elastically and structurally inhomogeneous solid." Journal of Applied Physics 92.3 (2002): 1351-1360.

[17] Marconi, V. I., and E. A. Jagla. "Diffuse interface approach to brittle fracture." Physical Review E 71.3 (2005): 036110.

[18] Spatschek, Robert, et al. "Phase field modeling of fast crack propagation." Physical review letters 96.1 (2006): 015502.

[19] Karma, Alain, and Alexander E. Lobkovsky. "Unsteady crack motion and branching in a phase-field model of brittle fracture." Physical review letters 92.24 (2004): 245510.

[20] Henry, Hervé, and Herbert Levine. "Dynamic instabilities of fracture under biaxial strain using a phase field model." Physical review letters 93.10 (2004): 105504.

[21] Henry, H. "Study of the branching instability using a phase field model of inplane crack propagation." EPL (Europhysics Letters) 83.1 (2008): 16004.

[22] Miehe, Christian, Fabian Welschinger, and Martina Hofacker. "Thermodynamically consistent phase-field models of fracture: Variational principles and multi-field FE implementations." International Journal for Numerical Methods in Engineering 83.10 (2010): 1273-1311.

[23] Miehe, Christian, and Lisa-Marie Schänzel. "Phase field modeling of fracture in rubbery polymers. Part I: Finite elasticity coupled with brittle failure." Journal of the Mechanics and Physics of Solids 65 (2014): 93-113.

[24] Bazant, Zdenek P. Scaling of structural strength. Elsevier, 2005.

[25] Griffith, A. A. “The Phenomena of Rupture and Flow in Solids,” Philosophical Transactions of the Royal Society (London), 221 (1921), pp. 163–198.

[26] Hoagland, R. G., J. D. Embury, and D. J. Green. "On the density of microcracks formed during the fracture of ceramics." Scripta Metallurgica 9.9 (1975): 907-909.

[27] Evans, A. G., and Y. Fu. "Some effects of microcracks on the mechanical properties of brittle solids—II. Microcrack toughening." Acta Metallurgica 33.8 (1985): 1525-1531.

[28] Hutchinson, John W. "Crack tip shielding by micro-cracking in brittle solids." Acta metallurgica 35.7 (1987): 1605-1619.

CHAPTER 3. HIGHLY STRETCHABLE DOUBLE-NETWORK COMPOSITE AND ITS THEORY

3.1 Introduction

Embracing both high strength and high toughness while containing up-to 90% of water, double-network (DN) hydrogels have drawn much attention in the last decade,[1-6] and have been demonstrated in potential applications ranging from smart structures to biomedical engineering.[6-8] From a structural perspective, a DN gel can be regarded as a molecular composite consisting of two interpenetrating polymer networks besides water: one with relatively short and stiff chains (the 1st network) and the other with much longer and initially coiled chains (the 2nd network). When compositionally and structurally optimized, the toughness of the DN gel could reach several orders of magnitude higher than a single network gel of either of the base polymer networks.[9] The toughening mechanism of DN gels has been attributed to the fragmentation and distributed damage in the 1st network.2 The 2nd network, which does not break until the 1st network is damaged in a large process zone in the surrounding area, stabilizes the fracture of the 1st network and preserves the overall integrity. Subject to uniaxial tension, DN gels often exhibit a yielding-like phenomenon with a plateau in terms of nominal stress, which could also be attributed to the partial damage and the coexistence of the damaged and undamaged zones.[10-11] Partially damaged DN gels almost fully recover the geometry upon unloading, while the hysteresis loop was found to be unrecoverable,[12] except for the DN gel with a self-healing ionic gel as the 1st network.[13] Various models have been developed to characterize the behavior of DN gels and explain the toughening mechanism,[11,12,14-18] although a few questions remain unclear, including the microscopic morphology in the partially damaged zones.

Inspired by the success of DN gels and the much better improvement over the base materials compared to conventional macroscopic composites, it is natural to wonder whether similar toughening mechanisms can be applied to the development of tough composites with different materials or in larger scales. In the current study, by combining a stiff but brittle fabric mesh and a soft acrylic tape, a highly stretchable and tough DN composite was designed and fabricated. The two constituents served the same purpose as the two networks in a DN gel: the fabric mesh provided the stiffness and strength, and served as the sacrificial just as the 1st network of a DN gel, and the acrylic tape served as the ductile substrate, just like the 2nd network. The two materials were initially well bonded, but exhibited significant sliding after the fracture and fragmentation of the mesh, which enabled distributed partial damage in the mesh. In this study, the mechanical properties of the composite were investigated through both tensile and fracture tests. During uniaxial tension tests, a plateau on the nominal stress curve and a stable necking behavior similar as those in DN gels were observed. Under cyclic loading, due to the partial damage in the mesh and the finite sliding between the mesh and tape layers, the composite exhibited a significant hysteresis over the stress-stretch curves. In the fracture tests of pre-cracked samples, a large process zone formed near the crack tip by fragmenting the fabric mesh to resist facile propagation of the crack. With the optimized composition, the DN composite can be as strong as the mesh, and as stretchable as the tape. The fracture toughness is significantly higher than either of the base materials. To further understand the toughening mechanism of the composite and its relation to DN gels, a 1D shear-lag model is developed to study the damage evolution process. The model suggests that the finite sliding over the interface between the mesh and the tape layers serves as the key to the energy dissipation and damage-distribution

mechanisms of the DN composite. The model also predicts the stress-stretch relation of the DN composite with various compositions, the results agree well with experiments.

Even though the base materials chosen here may not be the best to compose the DN composite, the results demonstrate the possibility of constructing novel macroscopic composites by using the toughening mechanism of DN gels. On the other hand, the DN composite itself may be deemed as a macroscopic model for the study of DN hydrogels.

It should also be noted that numerous experimental studies have been carried out very recently on various types of composites by combining micro- or macroscopic fibers and hydrogels, especially tough hydrogels.[19-22] While all of these composites utilizes similar types of constituents as the one presented in the current paper: a stiff fiber network and a soft matrix, most of them do not exhibit the same DN-gel-like damage-distribution mechanism. Instead, toughening mechanisms which are commonly seen in conventional fiber-reinforced composites,[23] such as fiber pullout,[19,22] were observed. The typical stress-strain curve of most fiber-hydrogel composites shows a monotonic decrease after the peak load,[20,22] which corresponds to the rupture of the stiffer fibrous network, indicating a single fracture event in the fibrous network, rather than the distributed damage of the current DN composite as will be shown in the Experimental section. Nevertheless, the lack of the toughening mechanism is more likely because the required conditions are not met, as will be discussed in the Theory section. When proper structural or material parameters are taken, some of these hydrogel composites may also exhibit similar behaviors.

3.2 Experimental

3.2.1 Sample fabrication and testing

The DN composite samples were prepared by stacking a nylon fabric mesh (mesh size approximately 1.9 mm, and wire thickness approximately 0.2mm) with hexagonal grids alternatingly with layers of VHB acrylic tapes (3M 4910, unless otherwise stated), as illustrated by Fig. 3.1a. The sticky nature of the VHB tapes enabled the easy bonding between the fabric mesh and the tape without additional adhesive.

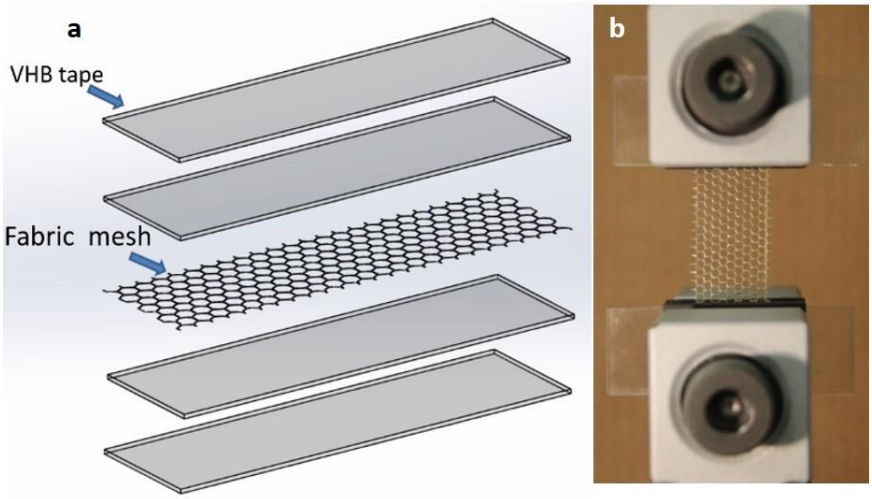

Figure 3.1. *(a) Sketch of the fabrication process of the DN composite. (b) Photograph of a test sample of DN composite gripped between acrylic glass slides.*

The mechanical tests were carried out over an Instron 5960 dual column testing system. Acrylic glass slides were then used to mount the samples for testing, as shown by Fig. 3.1b. By testing identical samples at various loading rates (15, 30, 60, and 120 mm/min), the strain-rate dependence of the mechanical properties of the composite was found to be negligible, although the VHB tape is known to be viscoelastic. The primary loading rate used for most tests was a constant extension rate of 30mm/min for repeatable

results and minimal data noise from the loading system. The samples were loaded to a total extension distance of up to 700mm or until rupture. A high-speed camera was used to investigate the damage evolution in the composite and the process of crack propagation.

In the uniaxial tensile tests, each sample was cut into a 25mm×50mm rectangular shape (50mm was the gauge length). As the mesh layers added negligible thickness to the composite, the sample thicknesses were taken to be approximately the total thicknesses of the VHB tapes (at approximately 1mm each). The composition of each sample will be noted by the mesh-to-tape ratio, a:b, which indicates a layers of mesh for every b layers of VHB 4910 tape (or the equivalent number of layers to reach the same thickness if a different type is used). As references, samples of the base materials: the fabric mesh and the VHB tape alone, were cut into the same size and tested.

As pointed out by recent studies, the strength and toughness of a hexagonal mesh exhibit significant anisotropy.[24] Similarly, the DN composites also showed different performances along the two symmetry axes. The DN-gel like toughening mechanism as well as the similar composition dependences, on the other hand, can be observed in both directions. For clarity of presentation, only the results of the loading along the shorter axis of hexagon, which showed better performance in both stretchability and toughness, are presented in the following sections.

3.2.2 Uniaxial tension

A typical force-stretch curve of a DN composite (mesh-to-tape ratio 1:2) subject to uniaxial tension is shown in Fig. 3.2a, in comparison with those of the fabric mesh and VHB tape. Compared to the fabric mesh, the composite exhibited much higher extensibility (~600%), close to that of a VHB tape. The extensibility of the composite should be

attributed to the damage delocalization mechanism, as illustrated by Fig. 3.2b. Upon rupture of the mesh layer, large deformation was manifested locally by the tape layers, which carried the load and stabilized the damage localization. Subsequent damage in the composite took place in the mesh layer elsewhere, instead of in the bare tape layers. Ultimately, the accumulated partial damage coalesced and fragmented the mesh into islands connected by the tape layers, as shown by Fig. 3.2b. Such a process was very similar to what was believed to happen during the partial damage of DN gels,2 as sketched in Fig. 3.2b, although it had never been directly observed. Here, the mesh layers resembled the 1st network, while the tape layers served a similar purpose as the 2nd network in DN gels.

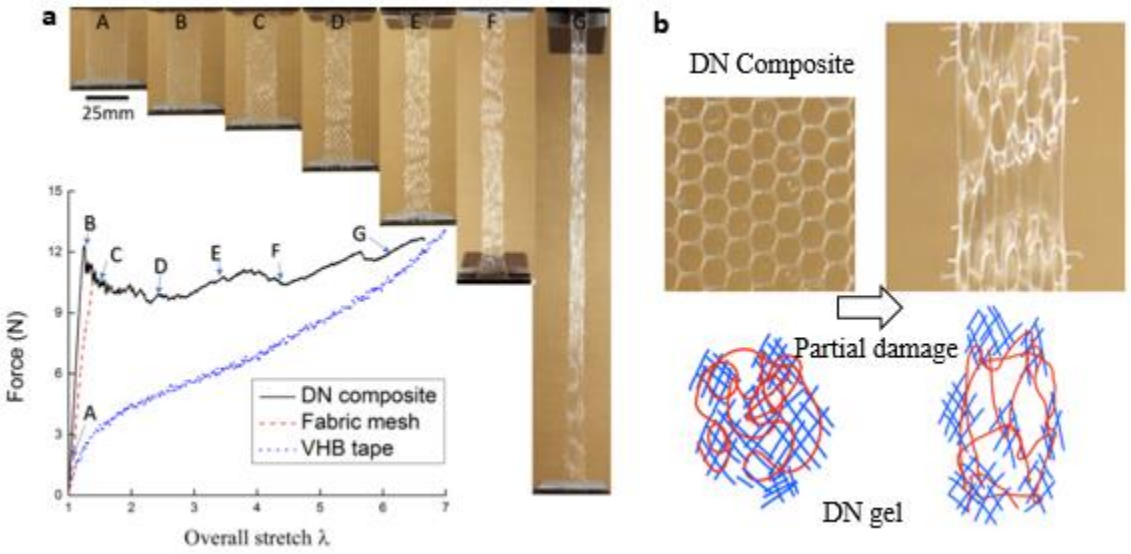

Figure 3.2 *(a) Force-stretch curves of a VHB tape, a fabric mesh, and the DN composite with 1 layer of mesh and 2 layers of VHB tape. For comparison, the force of the VHB tape was multiplied by 2 due to DN composite contains 2 VHB tape layers. The insets A-F are snapshots of the sample correspond to the specific points along the loading curves. Over the stress plateau (B-F), partially damaged regions coexisted with the undamaged regions, and the stretch was accompanied by the growth of the damaged regions. In the strain-hardening state (F-G), the entire sample was in a partially damaged state, and the stretch caused further sliding. (b) Comparison between the partial damage process in the DN composite and a similar mechanism in DN gels.*

To accommodate the large stretch, the deformation had to be non-affine between the mesh and the tape. The non-affinity was also shown by the traces of sliding of the mesh fiber between the tape layers. As will be demonstrated in the discussion follows, such sliding is essential in the toughening mechanism of the DN composite.

Similar as in DN gels, a typical force-stretch curve of the DN composite subject to uniaxial tension also exhibited three stages: (I) the initial stage of linear-elastic deformation, (II) the stress plateau, and (III) the strain-hardening stage before final rupture. Corresponding to the stress plateau was the coexistence of partially damaged zones with fragmented mesh and undamaged zones, as shown by the snapshots C through F in Fig. 3.2a. The phenomenon was similar to the stable necking propagation in a DN hydrogel,[10] although here the necking was mainly in the reduction of thickness due to the 2D planar nature of the samples. Over the stress plateau (stage II), further stretch was manifested by the growth of the partially damaged zones at the expense of undamaged zones. The structure in the partially damaged zones was hardly changed. At the end of stage II, the partially damaged zone covers the entire sample. In other words, the mesh in the entire sample was fragmented. In stage III that followed, the deformation was accompanied by further sliding between the mesh and tape layers.

To study the effect of composition, samples of various mesh-to-tape ratios were fabricated and tested. Figure 3.3 shows the measured stress-stretch curves of DN composite samples of various compositions under uniaxial tension. For comparison, the nominal stress was calculated by dividing the force by the cross-sectional area of the sample before deformation, while the overall stretch was the ratio between the deformed length and the original length. The results revealed consistent trends. Both the peak stress and the plateau

stress increased monotonically with the mesh-to-tape ratio. The stretch at which the strain hardening started also increased monotonically with the mesh-to-tape ratio, although the connection points between the plateau and strain-hardening regimes were not so clear due to the small hardening slope, especially at high mesh-to-tape ratios. The ultimate fracture strength was almost constant, independent of the composition. The fracture stretch decreased with the mesh-to-tape ratio. At low mesh-to-tape ratios, the fracture stretch was close to that of the VHB tape alone. These observations will be rationalized through a theoretical model in the Theory section.

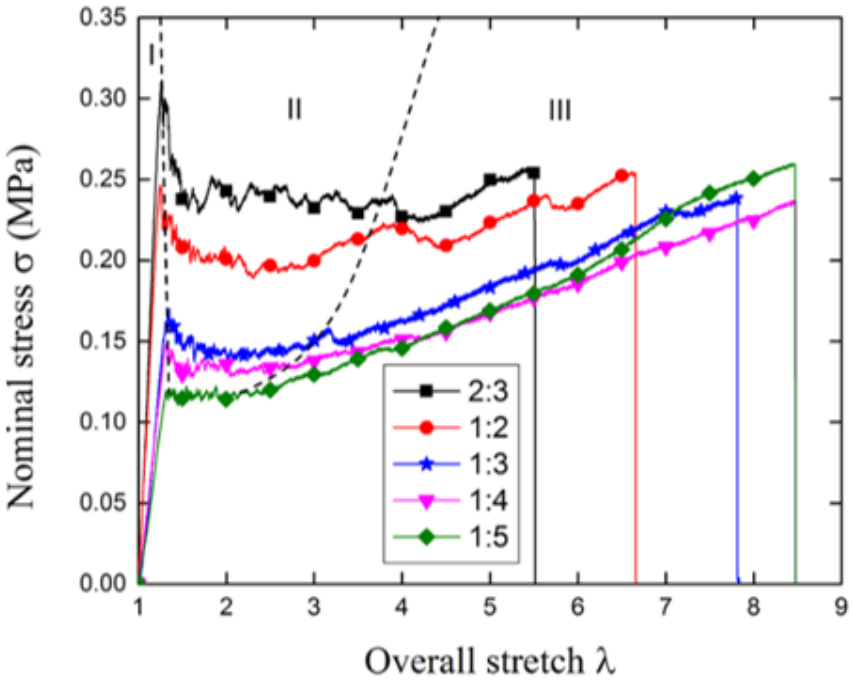

Figure 3.3. *Nominal stress-stretch curves of the DN composite at various compositions, from 2:3 to 1:5. The three stages are delimited roughly by the dashed lines.*

Loading-unloading behavior of the DN composite was also studied by testing samples of the same size as previously described. A representative result (of a 1:2 sample) is plotted in Fig. 3.4. Just like DN gels,[12] the stress-stretch curve exhibited significant hysteresis

when unloaded from stage II or III. Within a small error (20%-30% strain), the unloaded sample almost recovered its original length. When reloaded, the nominal stress also plateaued at approximately the same level as that prior to unloading. In contrast to the DN gels,[12] the reloading curves differed significantly from the unloading curves. The difference may be attributed to the substantial sliding forces between the mesh and the tape layers, which acted in opposite directions during loading and unloading.

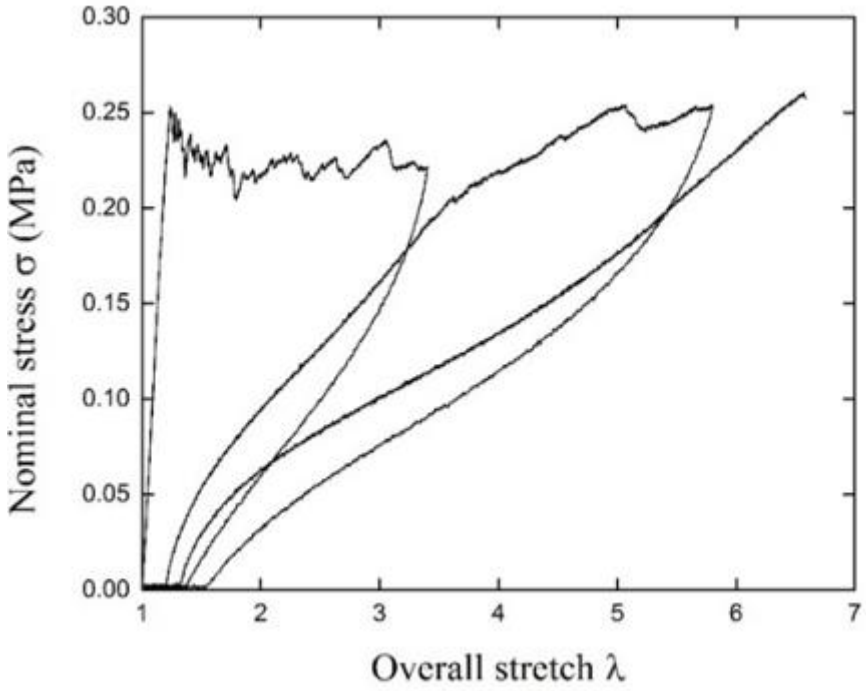

Figure 3.4. *Loading and unloading curves for a 1:2 DN composite sample subject to uniaxial tension.*

3.2.3 Fracture tests

Pre-cracked specimens of various compositions with the dimension of 100 mm × 100 mm were fabricated and subject to pure shear tests to study the crack tolerance of the DN composite. A 30 mm long edge crack was cut on one side of each specimen. Typical crack propagation and damage evolution processes are shown in Fig. 3.5, together with the results

of a VHB tape as a reference. The regions where the mesh layers have fractured, which roughly correspond to the fracture process zones of the DN composite, are delineated on the figures by dashed lines.

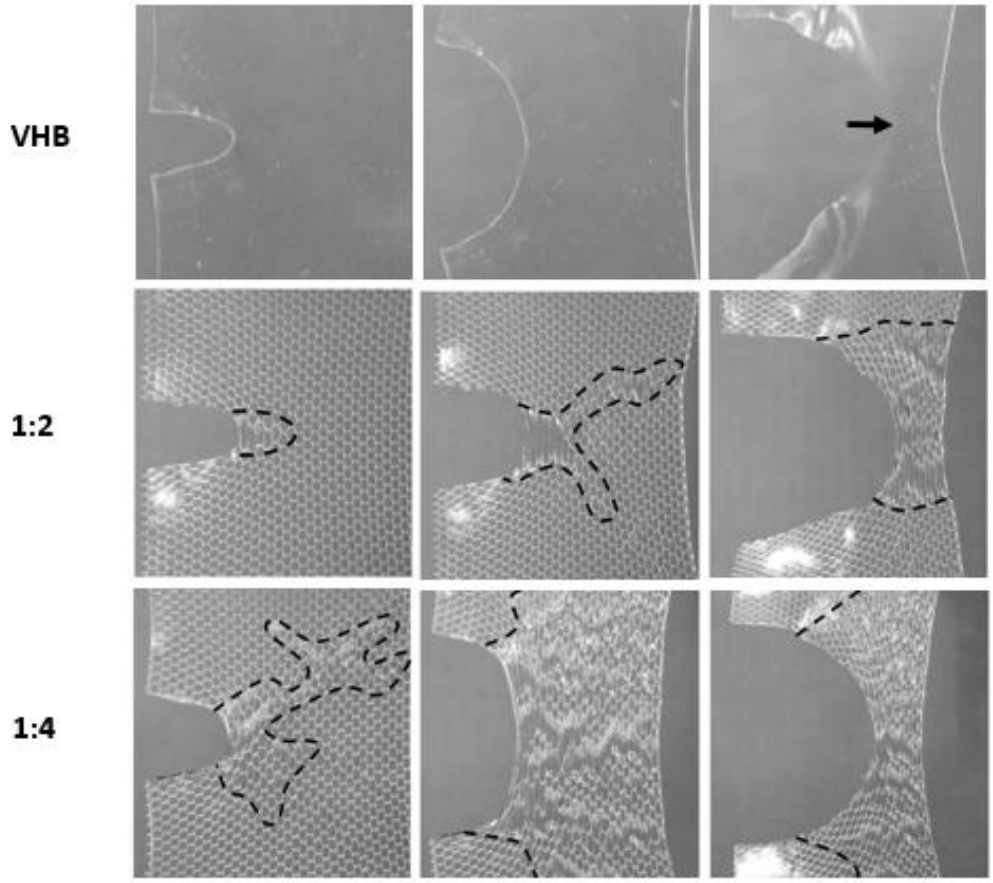

Figure 3.5. *Snapshots of the crack propagation and damage evolution in pre-cracked samples of the DN composite, together with the results of a VHB tape. The fracture process zones are encircled by the dashed lines. The arrow points at the crack tip of the VHB tape. The first snapshots were taken under the same stretch across the three samples. The second snapshots were taken at the moments when the cracks started to propagate. The third snapshots were captured during the crack propagation.*

The damage evolution in the DN composite samples followed two stages. The initiation of damage took place in the mesh layer at the tip of the pre-crack, at a relatively low stretch (~20% strain). The subsequent deformation was manifested by the growth of the

damage zone in the mesh layer. Most samples demonstrated significant crack blunting in this stage. In the second stage, the crack tip in tape layer propagated, followed by the collateral damage in the surrounding mesh, i.e. the fracture process zone. In the process zone, the initial damage pattern contained cracks perpendicular to the loading direction, and later turned into fragmented mesh surrounded by tape-only regions when the cracks collapsed. In the case when the second stage took over when the process zone was still smaller than the entire sample, e.g. the 1:2 case in Fig. 3.5, the crack propagation was accompanied by the traversing of the process zone throughout the sample. For samples with relatively low mesh-to-tape ratios, e.g. the 1:4 case in Fig. 3.5, the fracture process zone encompassed the entire sample prior to the crack propagation. Although the process zone could not grow further in this case, the crack propagation still involved further damage in the mesh layer, similar as that in stage III during uniaxial tension. In both cases, the cracks advanced slowly and stably, in contrast to the fracture of a VHB tape, in which the crack swept through the entire sample right after initiation.

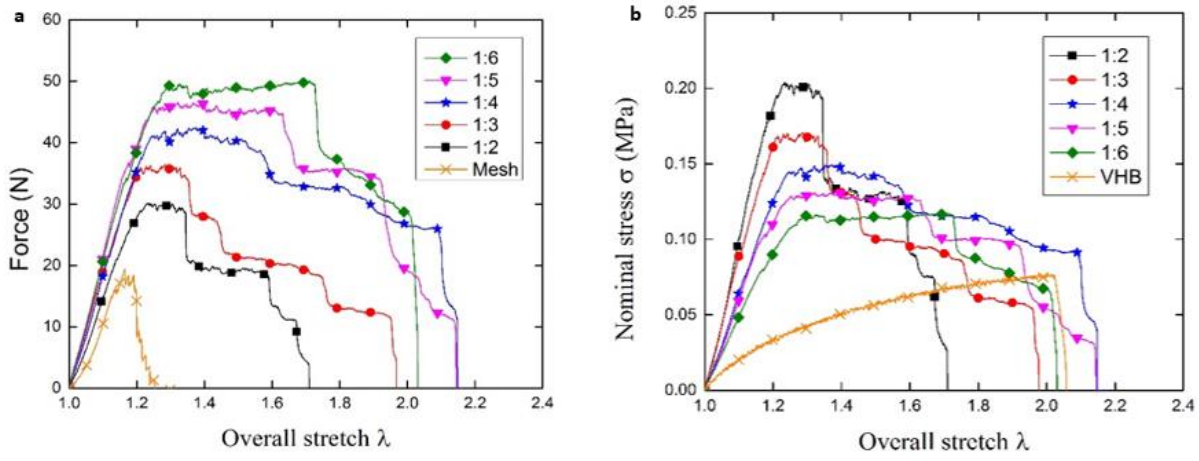

Figure 3.6. *(a) Force-stretch curves of pre-cracked samples of the DN composite at various compositions, compared to that of a mesh-only sample. (b) Nominal stress-stretch curves of pre-cracked samples at various compositions, compared to that of a tape-only sample.*

The fracture testing results of the DN composite with various compositions are plotted in Fig. 3.6. For clearer presentation and comparison with the base materials, the same set of data are plotted in two different ways: as force versus stretch in Fig. 3.6a, and nominal stress versus stretch in Fig. 3.6b. Compared to the mesh-only sample, the DN composite samples were tougher and much more stretchable. Compared to the VHB tape, the DN composite exhibited significantly higher strengths and its stretchability was comparable and even higher at some compositions.

To further compare the toughness of the composite among different compositions, the fracture work was calculated by integrating the area below each stress-stretch curve and multiplying by the sample height. As shown by Fig. 3.7, the fracture work of the DN composite is consistently higher than the VHB tape in all compositions, and is maximized at 1:4 when the overall fracture stretch is comparable or even higher than the VHB tape. The fracture work results were consistent with those obtained from the uniaxial tension tests, and with the fracture performance of DN gels in trend [25-26]: In general, DN gels have the highest fracture toughness when the molar concentration of the 2nd network is at some intermediate level.

It should be noted that due to the large process zone size, the data obtained could not be taken directly as the fracture toughness of the composite. It is expected that the measured values were size dependent, and an even higher fracture work could be achieved over a larger sample. Even though such studies are not included in the current paper due to the limited sizes of the base materials available, it is evident that the DN composite is very crack tolerant.

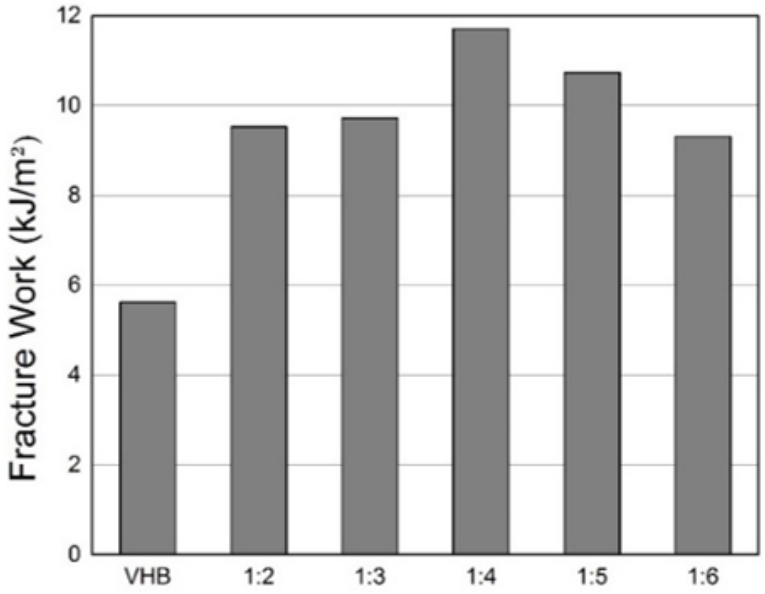

Figure 3.7. *Fracture work of pre-cracked samples of VHB tape and DN composite with various compositions as indicated.*

3.3 Theory

To rationalize the high toughness of the DN composite, we propose the following model for the damage distribution and energy dissipation process. For simplicity, the deformation is assumed to be uniaxial, and the damage only breaks the mesh along the transverse direction. As suggested by the stress-stretch curves from experiments (Fig. 3.3), the deformation process of a DN composite can be divided into three stages. Stage I is experienced only during the first loading, or the reloading after unloaded from any state in stage I.

In stage I, prior to any damage, the deformation is fully recoverable and is coherent between the mesh and the tape. The behavior of the composite is close to linear elastic, and the effective nominal stress σ is related to stretch λ by the rule of mixture:

$$\sigma \approx \left(\frac{k}{H} + 3\mu \right)(\lambda - 1) \tag{3.1}$$

where k is the effective tensile stiffness of the mesh (in a dimension of force per unit length), H is the undeformed thickness of the tape layers, and μ the initial shear modulus of the VHB tape. By writing Eq. (1), the thickness of the mesh layer is neglected and the thickness of the composite is assumed to be identical to that of the constituting VHB tapes. Stage I ends at the damage initiation of the mesh, when its membrane force reaches the strength f^* of the mesh: $k(\lambda - 1) = f^*$. Here for the mesh, the membrane force f (i.e. force per unit width of the sample) is chosen in place of stress to avoid the hassle of defining the thickness of a mesh layer. The corresponding peak nominal stress in the composite is given by

$$s_{\text{peak}} \approx \frac{f^*}{H}\left(1 + \frac{3\mu H}{k}\right). \tag{3.2}$$

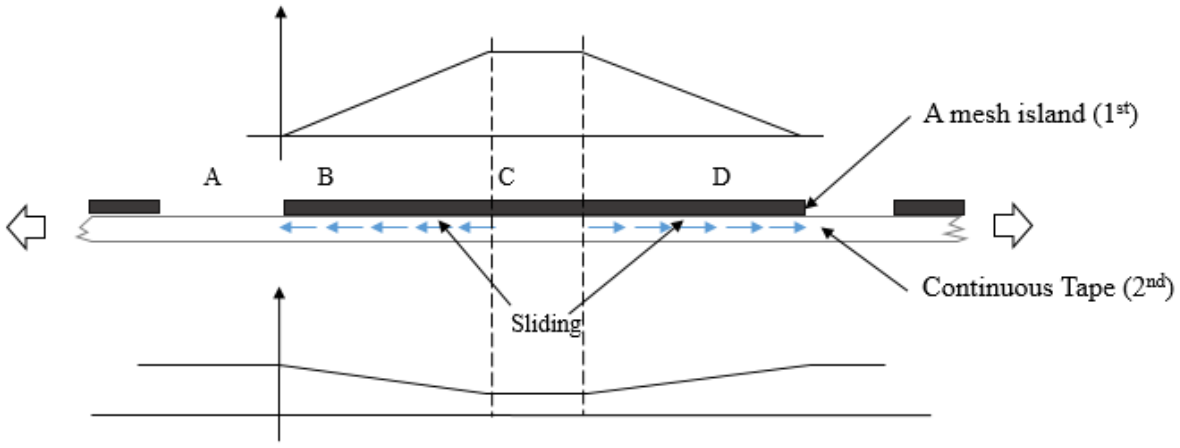

Figure 3.8. *Sketch illustrating the interaction between the mesh and the tape. The membrane force/stress distribution in the mesh and tape layers. The mesh acts like the 1st network in a DN gel, while the tape acts like the 2nd network.*

After reaching the peak stress, crack initiates in the mesh layer, and the deformation of the DN composite is in stage II. For the DN-toughening mechanism to work, it is essential

to have the partially damaged mesh (the 1st network) to fragment further rather than the tape (the 2nd network) to fracture under an existing crack of the mesh. Let us consider a partially damaged state of the composite, as sketched in Fig. 3.8. The mesh is fragmented into discontinuous islands, while the underlying VHB tape is still in one piece. The interaction between the mesh and the tape, as well as the stress and force distribution in each layer, are sketched in Fig. 3.8. For illustration, only one layer of each is shown. A relatively large island of the mesh can be divided into three regions along the loading direction. On each side of the island, there is a region of interlayer sliding (B and D on Fig. 3.8). In the middle of a large enough island, there is a center region where no interlayer sliding takes place and the mesh and the tape deform coherently (C on Fig. 3.8). The sizes of the side and center regions are denoted by L and r in the deformed configuration, respectively. A transition zone, which scales with the thickness of the tape, connects between the two regions. In the current paper, however, the effect of the transition zone is neglected. Despite the discrete nature of the mesh layer, the membrane force f is defined as a continuum quantity, homogenized over a region larger than a mesh grid.

Due to the interlayer sliding, a shear stress is present between the mesh and the tape, which transfers the axial load gradually between the mesh and the tape, as sketched in Fig. 3.8. Here for simplicity, we approximate this interaction by a shear-lag model with constant shear stress τ per deformed area. Under such an assumption, the resulting axial stress and force distributions in the mesh and the tape are qualitatively shown by Fig. 3.8. The stress in the tape maximizes in zone A where the bare tape is exposed due to sliding, and the membrane force in the mesh is maximized in the middle of each island, zone C. For effective energy dissipation, the force in the mesh at zone C should reach the tensile strength

f^*, while that in the tape at zone A should be below the strength of the tape $\sigma < s_{\text{tape}}$. Otherwise, the tape and consequently the entire composite will rupture at zone A, and the fracture process will be more like those of some fiber-reinforced hydrogels. Such a requirement sets the size of the sliding zone (B and D) in a steady state,

$$L_s \approx \frac{f^*}{\tau}. \tag{3.3}$$

When some mesh islands larger than $2L_s$ still exist, they will further break into smaller islands at the same peak stress s_{peak} given by Eq. (3.2), and the deformation of the DN composite proceeds in stage II. When all the islands are smaller than $2L_s$, nowhere in the composite will have coherent interface, and the deformation will go into stage III.

The importance of the interlayer sliding and the non-affine deformation between the mesh and the tape layers could be understood as follows. If the bonding is perfect without any sliding at the interface, the size of zone A will be infinitesimal as no tape will be stretched out from beneath the mesh. Obviously, zone B or D will not exist either. Consequently, the overall strain of the composite equals approximately that in zone C, which is bounded by the maximum strain of the mesh prior to fracture. As a result, the composite will have very limit stretchability even if the mesh could fragment into a number of islands. The role of interlayer sliding in the DN composite is similar to that of the pullout of the 2nd network from the damaged 1st network in a DN gel. [11]

Accompanied by the damage evolution in stage II, a DN composite should experience some stick-slip-like events, each of which corresponds to a drop in stress due to the rupture of one mesh island, followed by an increase due to the sliding and reloading of the tape layer under the cracked region, as shown by the schematic stress-stretch curve on Fig. 3.9.

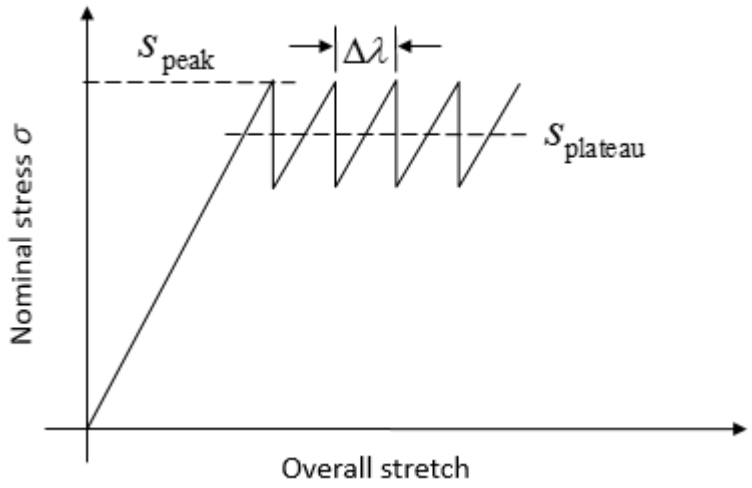

Figure 3.9. *Sketch of the stick-slip behavior due to the discrete nature of the nature, in stage II of the DN composite under uniaxial tension.*

The peak stress is obviously bounded by s_{peak}, and the discrete increment in the overall stretch $\Delta\lambda$ is associated with the length of sliding L_s related to the overall size of the sample D: $\Delta\lambda \approx 2\lambda_s L_s / D$, where λ_s is the average stretch in the tape at the sliding zones (A, B, D). Given that the resultant force transferred by a sliding zone is f^*, we can obtain the approximate scaling law for the average stretch $\lambda_s \approx \alpha f^* / \mu H$, with α being a numerical factor. In reality, the damping caused by the viscoelasticity of the tape or the interlayer adhesion will smooth out the stick-slip events and result in a plateau of almost constant stress. The plateau stress $s_{plateau}$ can be estimated from an energy perspective, e.g. by achieving the same area below the stress-stretch curve, as sketched in Fig. 3.9. Neglecting the stiffness change caused by the mesh fracture, we can estimate the difference between the peak stress and the plateau stress as

$$s_{peak} - s_{plateau} \approx \frac{\Delta\lambda}{2}\left(\frac{k}{H} + 3\mu\right) \approx \frac{f^*}{\mu H}\left(\frac{k}{H} + 3\mu\right)\frac{L_s}{D}. \tag{3.4}$$

From Eq. (3.4), the effect of interlayer sliding may be further appreciated. Although the interfacial shear stress τ does not appear explicitly in the final result, it affects the sliding-zone size L_s through Eq. (3.3). A lower sliding stress corresponds to a larger sliding zone, and thus a lower plateau stress s_{plateau} as given approximately by Eq. (3.4). On the other hand, if the sliding stress is high, although a higher plateau stress can be reached, the ultimate overall stretch is reduced. Therefore, an intermediate interlayer sliding stress is preferred for the DN composite to achieve optimal toughness.

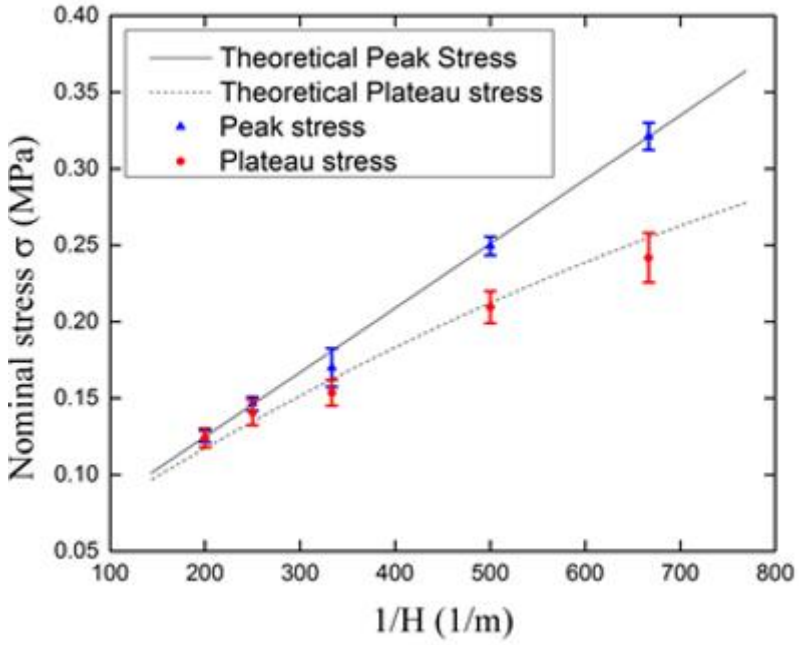

Figure 3.10. *The peak stress and plateau stress of the DN composite, plotted as functions of the inverse of the tape thickness, $1/H$. The dots show the experimental data, and the curves show the estimation from theory. The error bars indicate the range of data.*

Here, we take the values measured from independent experiments done over the mesh and tape individually: $k = 1170$ Nm^{-1}, $f^* = 420$ Nm^{-1}, and $\mu = 38$ kPa, and plot the peak and plateau stresses given by Eqs. (3.2) and (3.4) in Fig. 3.9. The unknown ratio L_s/D,

together with the numerical factor α, is taken to be a fitting parameter for the plateau stress. It is found that when the value $\alpha L_s / D \approx 0.01$ is taken, the plateau stress predicted by theory matches well with that measured, as shown by Fig. 3.10.

In stage III, as all mesh islands are smaller than $2L_s$, the maximum membrane force in the mesh is always lower than f^*. Therefore, no further damage will take place in the mesh layer, and the deformation is manifested by the interlayer sliding and the stretching of the tape layers. The overall nominal stress of the composite will continue to increase, until the maximum stress in the tape layer (zone A) reaches the ultimate strength of the tape. Due to the inhomogeneous deformation, the nominal stress at fracture of the DN composite is slightly lower than that of the VHB tape alone. To capture the stress-stretch relation in stage III, the detailed stretch distribution in the sliding zones is carried out by analyzing the axial force balance, as detailed in the Electronic Supplementary Information. The results are plotted in Fig. 3.11, together with the model predictions on the first two stages of deformation. To construct the stress-stretch curves, an incompressible neo-Hookean material law is assumed for the VHB tape, and an ultimate strength of $s_{\text{tape}} = 0.26\,\text{MPa}$ is taken. Compared to the experimentally measured stress-stretch curves (Fig. 3.3) across all compositions, the agreement is satisfactory. It could be seen that the measured slops of the strain-hardening segments (stage III) is lower than those given by the model. This is because the actual partial damage mode is 2D instead of 1D, i.e. the mesh layer fragments into randomly distributed islands of aspect ratios close to 1, rather than stripes perpendicular to the loading direction. Such a damaged phase is obviously more compliant than that in a 1D form.

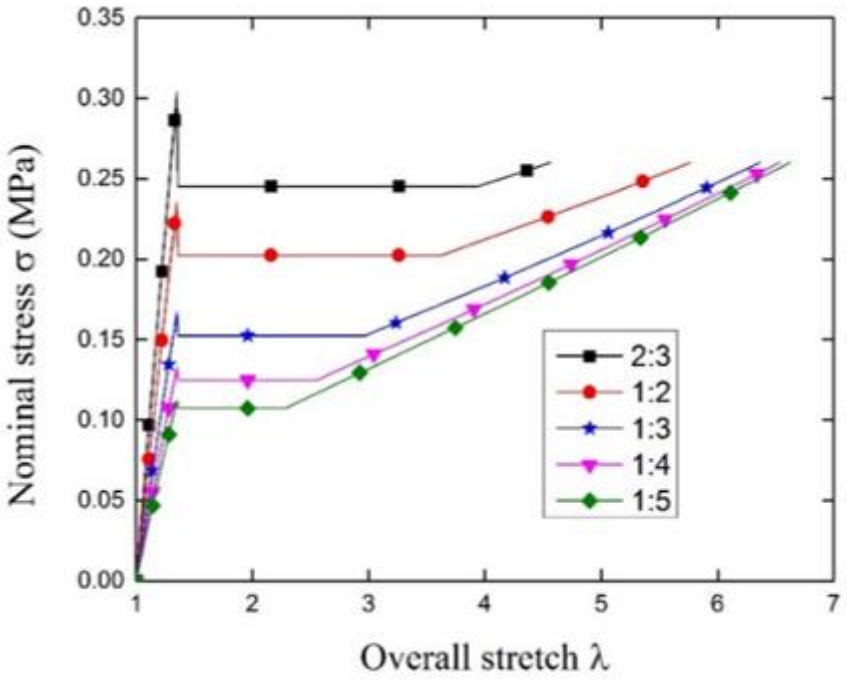

Figure 3.11. *Stress-stretch curves of the DN composite as predicted by the theoretical model. The five curves have the same mesh-to-tape ratios as the corresponding ones in Fig. 3.3. Detailed derivation is given in the Electronic Supplementary Information, and the material parameters are extracted from independent experiments on the base materials individually.*

3.4 Conclusions

By using a fabric mesh and a VHB acrylic tape, a soft but highly stretchable DN composite was manufactured and its mechanical properties tested. The DN composite followed very similar damage-distribution and toughening mechanisms as in the well-known DN hydrogels: it exhibited a stable necking phenomenon during uniaxial tension, it possessed large hysteresis during cyclic tensile tests and dissipated significant amount of damage, and it showed good crack tolerance. The DN composite was as strong as the mesh, as stretchable as the tape, and significantly tougher than either materials. The deformation and damage evolution process in the DN composite can be divided into three stages: the initial elastic stage prior to any damage, the stress plateau stage corresponding to the damage

propagation in the mesh layer, and the strain-hardening stage in which the deformation is manifested mainly by interlayer sliding. To capture the damage evolution process and to better understand the toughening mechanism, a theoretical model is developed by assuming 1D deformation and damage. The finite interlayer sliding is represented by a shear-lag model. With very few parameters obtained from independent tests over the base materials, the theory predicts the stress-stretch curves that agree well with the experiments in all compositions.

The DN composite, on the other hand, can be regarded as a macroscopic model for the study of DN hydrogels. Through visualizing the damage evolution and correlating the macroscopic properties with the underlying structures, it may provide insights towards the further optimizing of DN hydrogels for enhanced properties.

3.5 References

[1] Gong, Jian Ping, et al. "Double-network hydrogels with extremely high mechanical strength." Advanced materials 15.14 (2003): 1155-1158.

[2] Gong, Jian Ping. "Why are double network hydrogels so tough?." Soft Matter 6.12 (2010): 2583-2590.

[3] Nakayama, Atsushi, et al. "High mechanical strength double-network hydrogel with bacterial cellulose." Advanced Functional Materials 14.11 (2004): 1124-1128.

[4] Yasuda, Kazunori, et al. "Biomechanical properties of high-toughness double network hydrogels." Biomaterials 26.21 (2005): 4468-4475.

[5] Tsukeshiba, Hiroyuki, et al. "Effect of polymer entanglement on the toughening of double network hydrogels." The Journal of Physical Chemistry B 109.34 (2005): 16304-16309.

[6] Azuma, Chinatsu, et al. "Biodegradation of high-toughness double network hydrogels as potential materials for artificial cartilage." Journal of Biomedical Materials Research Part A: An Official Journal of The Society for Biomaterials, The Japanese Society for Biomaterials, and The Australian Society for Biomaterials and the Korean Society for Biomaterials 81.2 (2007): 373-380.

[7] DeKosky, Brandon J., et al. "Hierarchically designed agarose and poly (ethylene glycol) interpenetrating network hydrogels for cartilage tissue engineering." Tissue Engineering Part C: Methods 16.6 (2010): 1533-1542.

[8] Rakovsky, A., et al. "Poly (ethylene glycol)-based hydrogels as cartilage substitutes: Synthesis and mechanical characteristics." Journal of applied polymer science 112.1 (2009): 390-401.

[9] Haque, Md Anamul, Takayuki Kurokawa, and Jian Ping Gong. "Super tough double network hydrogels and their application as biomaterials." Polymer 53.9 (2012): 1805-1822.

[10] Na, Yang-Ho, et al. "Necking phenomenon of double-network gels." Macromolecules 39.14 (2006): 4641-4645.

[11] Wang, Xiao, and Wei Hong. "Pseudo-elasticity of a double network gel." Soft Matter 7.18 (2011): 8576-8581.

[12] Webber, Rebecca E., et al. "Large strain hysteresis and mullins effect of tough double-network hydrogels." Macromolecules 40.8 (2007): 2919-2927.

[13] Sun, Jeong-Yun, et al. "Highly stretchable and tough hydrogels." Nature 489.7414 (2012): 133.

[14] Lake, G. J., and A. G. Thomas. "The strength of highly elastic materials." Proc. R. Soc. Lond. A 300.1460 (1967): 108-119.

[15] Tanaka, Yoshimi, Koji Fukao, and Yoshihisa Miyamoto. "Fracture energy of gels." The European Physical Journal E 3.4 (2000): 395-401.

[16] Brown, Hugh R. "A model of the fracture of double network gels." Macromolecules 40.10 (2007): 3815-3818.

[17] Tanaka, Yoshimi. "A local damage model for anomalous high toughness of double-network gels." EPL (Europhysics Letters) 78.5 (2007): 56005.

[18] Zhao, Xuanhe. "A theory for large deformation and damage of interpenetrating polymer networks." Journal of the Mechanics and Physics of Solids 60.2 (2012): 319-332.

[19] Illeperuma, Widusha RK, et al. "Fiber-reinforced tough hydrogels." Extreme Mechanics Letters 1 (2014): 90-96.

[20] Lin, Shaoting, et al. "Design of stiff, tough and stretchy hydrogel composites via nanoscale hybrid crosslinking and macroscale fiber reinforcement." Soft matter 10.38 (2014): 7519-7527.

[21] Visser, Jetze, et al. "Reinforcement of hydrogels using three-dimensionally printed microfibres." Nature communications 6 (2015): 6933.

[22] King, Daniel R., et al. "Extremely tough composites from fabric reinforced polyampholyte hydrogels." Materials horizons 2.6 (2015): 584-591.

[23] Bao, G., and Z. Suo. "Remarks on crack-bridging concepts." Applied Mechanics Reviews 45.8 (1992): 355-366.

[24] Ma, Zhuo, Xiangchao Feng, and Wei Hong. "Fracture of soft elastic foam." Journal of Applied Mechanics 83.3 (2016): 031007.

[25] Tanaka, Yoshimi, et al. "Determination of fracture energy of high strength double network hydrogels." The Journal of Physical Chemistry B 109.23 (2005): 11559-11562.

[26] Na, Yang-Ho, et al. "Toughening of Hydrogels with Double Network Structure." e-Journal of Surface Science and Nanotechnology 3 (2005): 8-11.

CHAPTER 4. A MAGNETIC DOUBLE-NETWORK COMPOSITE CAPABLE OF LARGE RECOVERABLE DEFORMATION

4.1 Introduction

Double-network (DN) gels and elastomers have been of great interest to researchers in the last decades for their superior mechanical characteristics including both high strength and high toughness [1-14]. The desirable features endow DN gels and elastomers with applications in various areas [8-15]. The toughness of DN gels and elastomers has been attributed to the interpenetrating network structures: the 1st network consists of relatively short and stiff chains while the 2nd network of long and highly coiled chains [2]. During loading, partial damage initiates in the 1st network. But the cracks in the 1st network are bridged by the chains of the 2nd network, which are gradually pulled out from the fragments of the 1st network to accommodate the large deformation. At an optimal composition when the partially damage phase is stronger than the virgin phase, further loading will distribute in the 1st network in the surrounding area rather than rupturing the 2nd network. Such a process results in a large process zone and energy is dissipated through breaking the 1st network and sliding between the two networks.

Although the toughening mechanism is, in general, similar to the crack-bridging in conventional composites, DN gels and elastomers excel with unparalleled large strain-to-fracture. One may naturally wonder whether the same DN toughening mechanism can be applied to macroscopic composite materials. As the afore-described mechanism is not limited to molecular scales, it is theoretically applicable to structures of all sizes. Recently, by using a fabric mesh in place of the 1st network, and an acrylic tape the 2nd network, a macroscopic composite has been demonstrated [10], confirming the applicability of the DN mechanism to macroscopic structures. Just like DN gels and elastomers with chemically

crosslinked 1st network [1, 6-7], the DN composite has reduced and irrecoverable stiffness and toughness once damaged [10]. In contrast, when reversible ionic crosslinkers are used in DN gels, they exhibit self-healing capability as the partially damaged 1st network recovers by reconnecting the broken crosslinks [16]. Similar behaviors have also been observed in other tough hydrogel systems such as polyampholytes and poly-ion composites [17-19].

Inspired by the salient self-healing capabilities of the ionic crosslinks in the tough gels, we designed and tested a magnetic DN composite capable of large and recoverable deformation in this work. In analogy to the reversible ionic crosslinks in self-healing hydrogels [16-19], permanent magnets were used as the sacrificial and reconnecting components in the composite. The magnets were initially connected into fibers which provided the composite relatively high stiffness. Under a critical axial tension, the magnets separated from each other in sequence, and transferred the load to the elastomeric matrix. Exhibiting a long plateau over the stress-strain curve, the damage evolution process was similar to that of DN gels and elastomers. The strength of the composite was limited by the magnetic attractions while the maximum stretch was limit by the stretchability of the matrix. The composite was significantly tougher than either of the constituents. Upon unloading, the magnetic attraction between neighboring magnetics held them back again and the composite's stiffness and strength were fully recovered.

Even though the base materials chosen for this experiment may not form the optimal DN composite, the results demonstrate the possibility of constructing novel macroscopic composites using the toughening mechanism of DN gels. Hypothetically replacing the permanent magnets with electromagnets, an adjustably tough DN composite could be a future iteration. By combining the properties of high-stretchability, re-healing, and high-

toughness, the DN composite is a viable candidate for many applications. This macroscopic model design has the potential to be refined for use in prosthetics such as tendons and even artificial skin. Additionally, this composite could possibly be used for inflatable structures that have been of great interest in the aerospace community.

4.2 Experimental setup and results

The magnetic DN composite samples were prepared by first pouring the well-mixed Polydimethylsiloxane (PDMS, WACKER SILICONES, unless otherwise stated) precursor solution around the chains of cylindrical permanent magnets of two different sizes (φ4mm×10mm, φ2mm×1mm) inside rectangular molds, as schematically illustrated by Fig. 4.1. Once fully cured, the PDMS-magnet samples were removed from the molds for testing. The mechanical tests were carried out with an Instron 5960 dual column testing system. Each sample was held vertically by metallic grips with the magnetic chains aligned in the loading axis. By testing identical samples at various nominal strain rates (0.0015, 0.003, 0.006, and $0.012\frac{1}{s}$), the rate dependence of the mechanical properties of the composite was found to be negligible. The primary loading rate used for most tests was a constant extension rate of $0.003\ \frac{1}{s}$ for repeatable results and minimal data noise from the loading system. Each sample was loaded to a total extension of up to 500 mm or until rupture. Additional cyclic load-unload tests were also conducted for various distances. A video camera was used to record the separation of magnet links and corresponding deformation processes. The composition of each sample will be noted by the arrangement of magnetic columns and number of spacer magnets used. For comparison, control samples of PDMS and magnetic columns were made into the same size and tested.

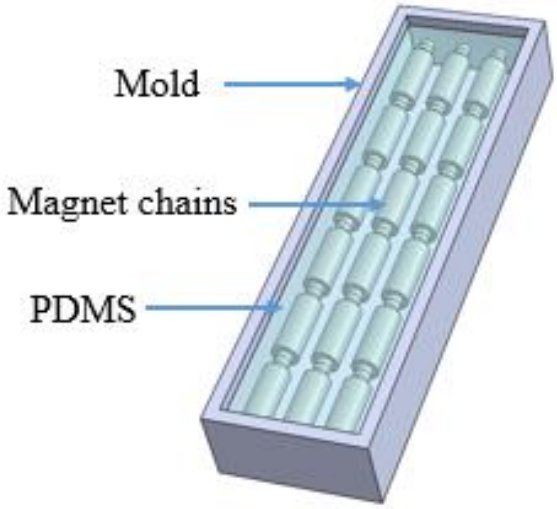

Figure 4.1. *Sketch of the manufacture process of the PDMS-magnets composite.*

A typical force–extension curve of a PDMS-magnetic DN composite subjected to uniaxial tension is shown in Fig. 4.2, together with the reference curves measured from the base materials. Compared to a single chain of magnets, the composite exhibited a much higher extensibility, close to that of the PDMS. The extensibility of the composite can be attributed to the damage-delocalization mechanism provided by the DN structure. Upon separation of each magnet link, large deformation was manifested locally by the PDMS, which carried the load and stabilized further damage localization. Here, the magnet chains resembled the 1st network of DN gels, while the PDMS is analogous to the 2nd network. To accommodate the large stretch, the deformation had to be non-affine between the magnets and the matrix. Similar to those of DN gels [2] and non-recoverable DN composites [20], a typical force–extension curve of the magnetic DN composite subjected to uniaxial tension also exhibited three stages: (I) an initial stage of linear-elastic deformation, (II) a relatively flat stress plateau with sawtooth patterns accompanying the separation events of individual

magnet pairs, and (III) a strain-hardening stage until final rupture. Corresponding to the stress plateau in stage II was the coexistence of two phases: a partially damaged phase with separated magnet links and an intact phase with connected magnet links, as shown by the insets of Fig. 4.2. No matrix (PDMS) damage is present in either phases. This phenomenon is like the stable necking propagation in a DN hydrogel [2] and previous DN composite research [10]. Over the stress plateau, further stretch was manifested by the growth of the partially damaged zones at the expense of the intact magnetic links. Stage II continued until all the magnets were separated. In stage III, deformation was accompanied by further stretching of the matrix and sliding between the magnets and the matrix.

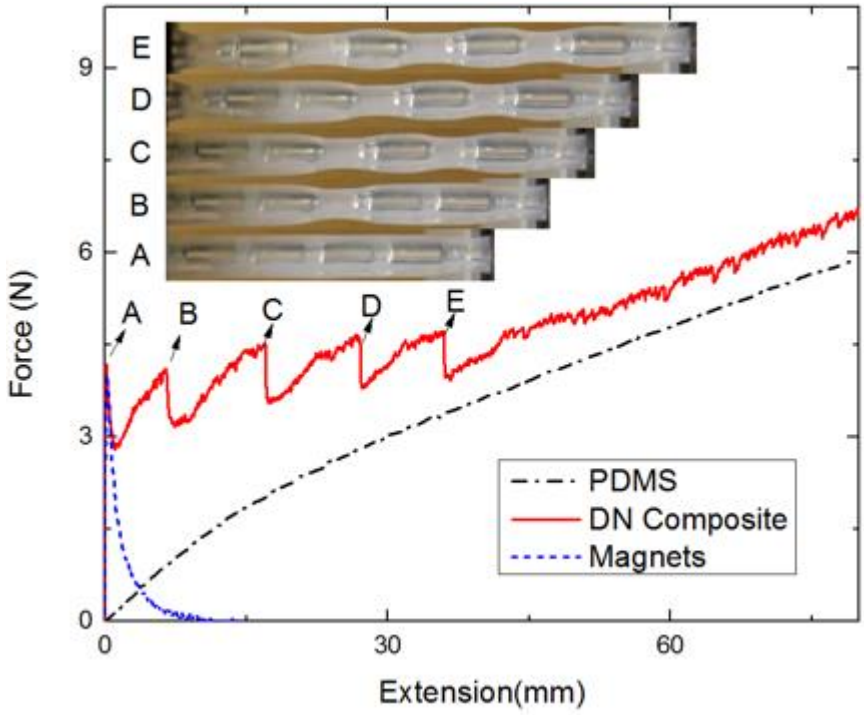

Figure 4.2. *Force-Extension curves of PDMS-Magnets composite, and DN composite with single chain of magnets. The insets A–E are the snapshots of the sample corresponding to the specific points along the loading curves. Over the stress plateau (A-E), partially damaged regions coexisted with the undamaged regions, and the extension was accompanied by the growth of the "damaged" regions. In the strain-hardening state, the entire magnet chain was separate, and the extension caused further sliding between magnets and PDMS.*

To study the effect of composition, samples of various number of chains and magnet volume fractions were fabricated and tested. Figure 4.3 shows the measured stress-strain curves of DN composite samples of various compositions under uniaxial tension, with the initial parts of the curves enlarged in the inset. The nominal stress was calculated by dividing the axial force by the cross-sectional area of the sample before deformation, while the Nominal strain was the ratio between the deformed length and the original length. The results revealed consistency across several sample tests. Both the peak stress and the plateau stress increased continuously with the magnet volume fraction. At low magnet volume fractions, the DN composite was closer to that of the PDMS only result.

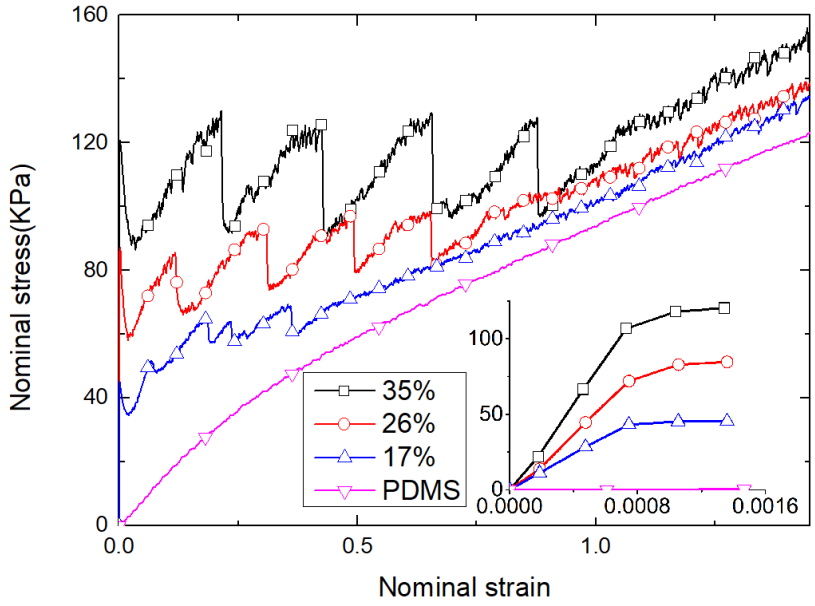

Figure 4.3. *Nominal stress-strain curves of DN composite at various compositions, from volume fraction 35% to 17%. The initial region curves with an exaggerated strain scale shown at bottom left.*

The hysteresis and energy dissipation of the DN composite were also studied by subject samples of various sizes to cyclic uniaxial tension tests at a set extension rate of

$0.003\,\frac{1}{s}$. By varying the number of magnetic columns in each sample, a range of effective magnet volume fractions was tested. A representative result (at a magnet volume fraction of 26%) is plotted in Fig. 4.4. Without a clear stress-plateau and the sawtooth patterns took place at much lower stress and strain levels, the unloading stress-strain curves appeared drastically different from the loading curves. The difference between loading and unloading curves induced large hysteresis in all cases when magnet links are separated. However, when reloaded, the nominal stress plateaued at approximately the same level as in previous cycles, indicating that both the stiffness and the strength of the composite were recovered. The small difference between loading and reloading curves might be attributed to the static interfacial adhesion between magnets and the PDMS matrix, which could be different from the friction force between the two when sliding took place. These observations will be further analyzed through a theoretical model in the following section.

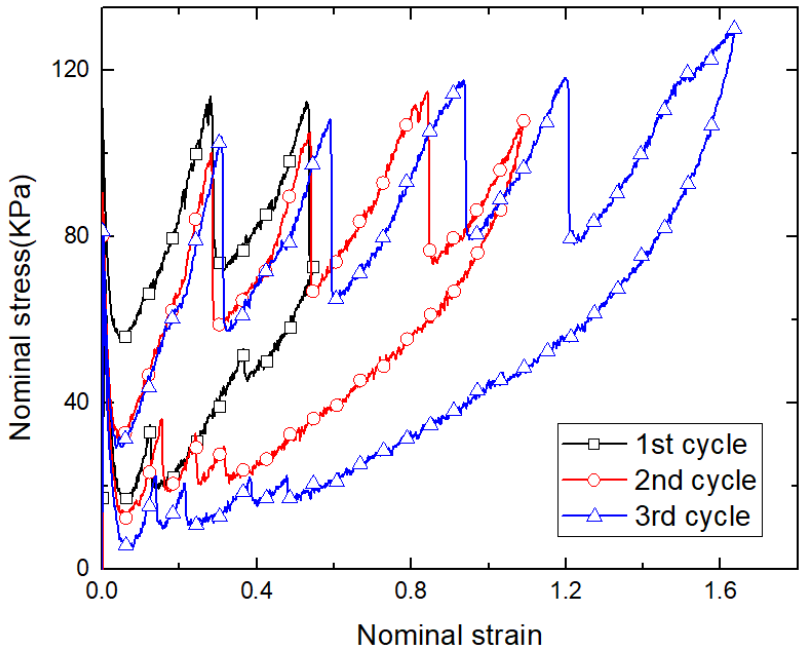

Figure 4.4. *Loading and unloading curves for a DN composite sample (volume fraction 26%) subjected to uniaxial tension.*

4.3 Theoretical

To rationalize the toughening mechanism of DN magnetic composite, let us consider a simple 1D model for the damage distribution and energy dissipation process. Each unit cell of the composite, which includes two (halve) magnets and surrounding PDMS matrix, is modeled as a pair of dipolar attractors and an elastic spring in parallel, as sketched in the inset of Fig. 4.5. With the magnetic attraction force modeled as dipolar attraction, and the behavior of the matrix as a nonlinear spring, the sliding friction or adhesion force between them are neglected in this simple model. The model simplification allows us to decompose the nominal axial stress into two parts: the elastic nominal stress s_e and magnetic nominal stress s_m.

The attractive force between two magnetic dipoles at distance r, with magnitude m and directions aligned along the axis, is given by

$$f_m = \frac{3\mu_0 m^2}{2\pi(r)^4} \tag{4.1}$$

Here the vacuum permeability μ_0 is used to approximate that in the PDMS matrix and in the air gap between magnets. Taking the center-to-center distance between a large magnets and stopper magnets as the effective dipolar distance, r is related to axial stretch λ and the undeformed length of a unit cell L as $r = L(\lambda - \frac{1}{2})$. Dividing the magnetic attraction by the undeformed cross-sectional area of a unit cell A, we obtain the magnetic nominal stress

$$s_m = \frac{3\mu_0 m^2}{2\pi A L^4 (\lambda - \frac{1}{2})^4} \tag{4.2}$$

While models are available for more accurate attractive forces between permanent magnets (e.g. ref. 21, 22, 23), the added mathematical complexity does not necessarily lead to a clearer physical picture for understanding. Here for simplicity, we just take the simple formulation of magnetic stress and neglect the magnetic interactions between non-neighboring magnets. The

magnetic nominal stress is always a monotonically decreasing function of the axial stretch, as shown by the dash curve in Fig. 4.5.

When a magnet link is disjointed, the surrounding PDMS matrix is stretched elastically, giving rise to an axial tension. For simplicity, we neglect the magnet-matrix interaction (adhesion or friction) and assume a uniform state of deformation with axial stretch λ in the matrix. By using an incompressible neo-Hookean material law with initial shear modulus μ, the elastic nominal stress is evaluated as:

$$s_{\mathrm{e}} = \mu \frac{A_{\mathrm{p}}}{A}\left(\lambda - \frac{1}{\lambda^2}\right), \tag{4.3}$$

where A_{p} is the effective cross-sectional area of the PDMS matrix in a unit cell.

The axial nominal stress in a unit cell of the composite is just the sum of the two contributions, $s = s_{\mathrm{m}} + s_{\mathrm{e}}$. In the following discussion, we further normalize all stresses by the magnetic stress in the undeformed state, $3\mu_0 m^2/2\pi AL^2$,and the dimensionless nominal stress now writes

$$\overline{s} = \frac{1}{\left(\lambda - \frac{1}{2}\right)^4} + \alpha\left(\lambda - \frac{1}{\lambda^2}\right). \tag{4.4}$$

The dimensionless parameter

$$\alpha = \frac{2\pi\mu A_{\mathrm{p}} L^4}{3\mu_0 m^2} \tag{4.5}$$

characterizes the significance of the matrix elasticity relative to the magnetic attractions. By fitting the experimental data of the magnets and PDMS individually, we obtain the parameter groups $3\mu_0 m^2/2\pi AL^4$ =5.4KPa and μ =3Kpa, $\alpha = 0.57$ for, for the samples of 26% PDMS volume fraction. The dimensionless nominal stresses are plotted as functions of the nominal strain $\varepsilon = \lambda - 1$ in Fig. 4.5.

It is noteworthy that the magnets are subject to an elastic compressive stress, which balances the magnetic stress (4.2) in the undeformed state. When an external axial tension is applied, the magnetic attraction is gradually carried over by the external force, and a minute extension takes place in the magnets as the elastic compression relieves. However, comparing to the compliant and stretchable PDMS matrix, the magnets are almost rigid and the elastic strains in the magnets negligible. The elastic part appears as an almost vertical segment on the stress-strain curve of the unit cell, as shown by Fig. 4.5.

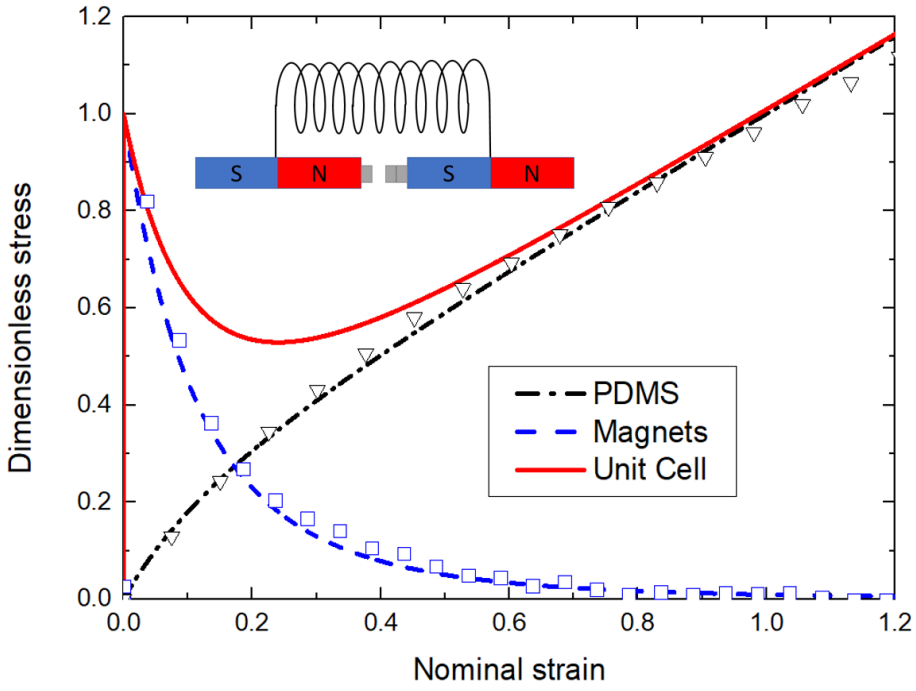

Figure 4.5. *Dimensionless stress-strain curves of one unit cell (26% volume fraction) as predicted by the theoretical model. The material parameters are extracted from independent experiments on the base materials individually. The experimental magnets data shows in blue square. The experimental PDMS data plot in black triangle.*

Let us now move on to multiple unit cells connected in series, and consider the three stages as in the stress-strain curve of a magnetic DN composite. In stage I, all magnet links are in the connected state, and the composite is in a linear elastic regime. If we neglect the

stiffness of the PDMS matrix and the change in the magnetic stress s_{m} at small strains, the stress-strain relation of stage I is given approximately by

$$s = \psi_m E \varepsilon \,, \tag{4.6}$$

where $\psi_{\mathrm{m}} \approx 1 - A_{\mathrm{p}} / A$ is the volume fraction of magnets, and E the Young's modulus of the magnets.

In stage II, some unit cells have the magnet links separated (the partially damaged state) while the rest are still connected (the intact state). Consider the case when there are N units in total and M of them are open. Neglecting the strain from elastically deforming the connected magnetic links, the overall stretch of the composite, $\bar{\lambda}$, is related to the local stretch λ in the partially damaged units by

$$\bar{\lambda} = \frac{M\lambda L + (N - M)L}{NL} = 1 + \frac{M}{N}(\lambda - 1), \tag{4.7}$$

By substituting Eq. (4.7) into Eq. (4.4), we arrive at the stress-stretch relation in all these states, as shown by the dash curves in Fig. 4.6. However, not all parts of these curves are stable.

Throughout loading, the axial stress is bounded by the peak value when the magnetic link separates in a single unit cell, $\bar{s} = 1$. When further stretched, one of the connected magnetic link will open, and the loading curve will jump to the next branch. Maximum magnetic stress between two magnets, f_0, beyond which an extra pair of magnets will be separated, then the loading curve will jump to the next one. In this paper, we neglect the dynamics and vibration of the system, and limit the discussion to the quasi-static cases, so that the jump occurs as a steep drop in force at constant elongation, as shown by Fig. 4.6. Such a process happens continuously during loading, until all magnet pairs are separated. This process

corresponds to a plateau with repeated ramps and drops on the loading curves of the composite. If all magnets are identical, the peak force of the ramps f_0 remains constant. A gradual increase of the peak force is observed in experiments. This is likely due to the non-uniformity of the magnets or the manufacturing defects of the composite structure (so that weaker links break earlier). And of course, the stiffening of PDMS also contributes to the larger stress.

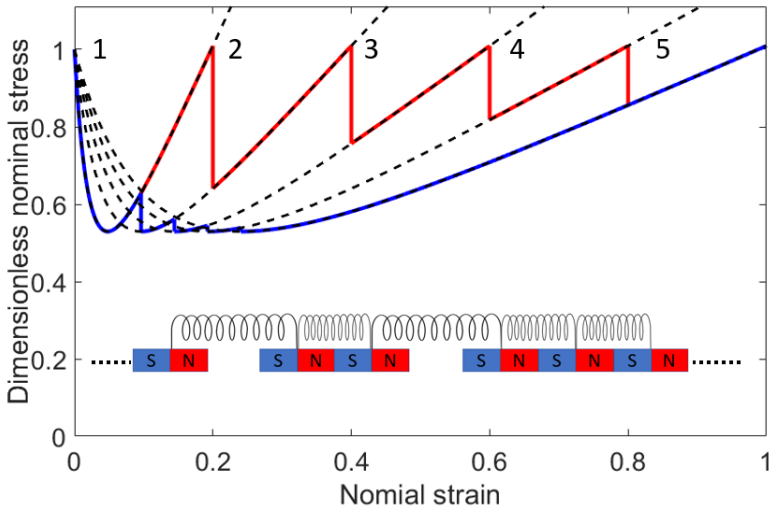

Figure 4.6. *Theoretical dimensionless stress-strain curves of one DN composite (26% volume fraction) for case when 1,2,3,4 and 5 pairs of magnets are separated. The sketch of magnets chain in bottom was indicate 2 unit cells are open.*

The composite behavior is different when the structure is unloaded. During unloading, the decreasing segments throughout the curves are all unstable. All separated unit cells will be relaxed uniformly until the trough of each branch of load-elongation curve is reached, and then one pair of magnets will snap into contact, and the curve jumps up to the previous branch of curves. The elongation at which the snap instability occurs is much lower than that of the separation during loading. The force needed to separate two magnets is much higher than the force two highly-separated magnets require to snap together. Such an asymmetry between loading and unloading results in a hysteresis over the stress-strain curve. This should be a

major mechanism for energy dissipation in the composite, as well as other structures and material systems with similar long-range forces that decrease with separation, e.g. electrostatic interaction. The troughs throughout the unloading curve are at a constant level. In reality, these decrease gradually during unloading, as shown by Fig. 4.6. The ramps and jumps on both the loading and unloading curves are caused by the discrete nature of the structure, and the overall smoothness is dependent on the number of unit cells in the system.

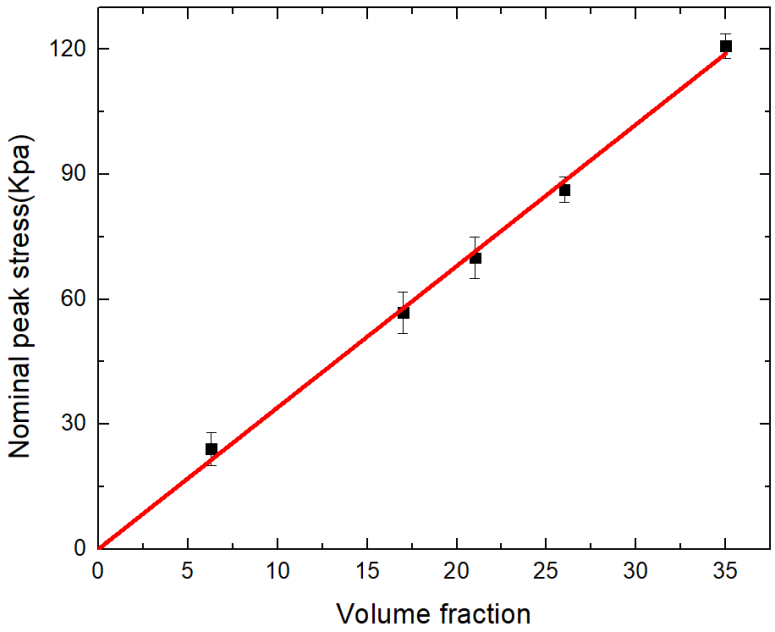

Figure 4.7. *The peak stress of DN composite, plotted as functions of volume fraction. The dots show the experimental data. And the curve shows the estimation from theory. The error bars indicate the range of data.*

The initial magnetic strength per unit area is defined as the stress when $\lambda = 1$,

$$s^* \approx \frac{24\mu_0 m^2}{\pi A L^4} \tag{4.8}$$

Here, the area of the magnets are the same: A_m. By varying the overall area of the composite, we can get experimental results for different magnet-volume ratios $\psi = \frac{A_m}{A}$. The magnetic

strength per unit area s^* should be proportional to the magnet-volume ratio : $s^* \propto \psi$. The experimental results are plotted in Fig. 4.7. The nominal peak stress of the composite shows a linear relation to the volume fraction of the magnets, which agrees with our theory.

In general, the nominal stress-overall strain curve of a unit cell of the composite is non-monotonic, containing three segments: the first part is an initially linearly increasing segment with a very large slope close to the rigidity of the magnets; the second part is the decreasing segment dominated by the declining magnetic attraction; and the third part is the increasing segment at large separation, dominated by the elastic force from the matrix. The minimum axial force marks the separation point of the second and third region. For a composite structure consisting of multiple unit cells in series, the first part is almost the same as the unit cell behavior, while the second part remains unstable. Throughout the decreasing region, the unit cells will randomly transit from all-contact states to all-separated states. After reaching the states that all magnets are separated, most of the force is carried over by the base material PDMS (third segment).

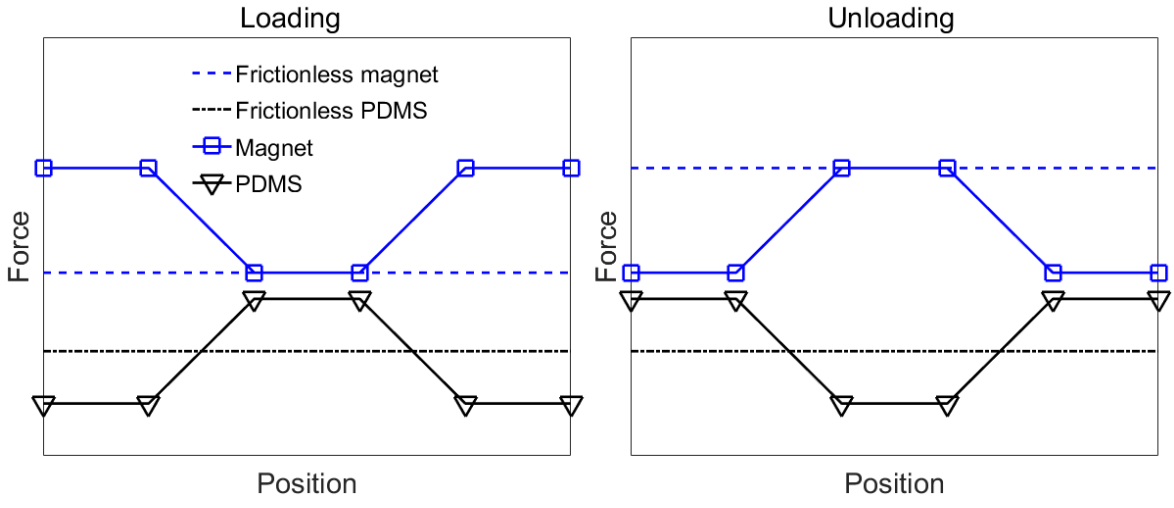

Figure 4.8. *Sketch illustrating the interaction between PDMS and magnets.*

In fact, the measured loading and unloading results slightly differ from the theoretical results. The loading curve stands on top of our theoretical curve while the unloading curve shows lower stress than our theoretical curve. We contribute these effects to bonding and friction within the composite. Imagine a frictionless case, in which the axial force of PDMS and magnets are uniform through the whole sample. Considering the self-recovery characteristic, the bonding between the PDMS and the magnets are always there, which endows the friction between PDMS and magnets. Similar to a previous proposed model[10], a sketch illustrating the interaction between the PDMS and magnets are shown in Fig.8. During testing, both ends of the PDMS and magnets are gripped together. There is a transition zone next to both ends where friction is present. For each loading step, the strain for the center part of the sample is larger than the one in the frictionless case, which gives a larger stress. While for the two ends, most of the axial force is carried over by the magnets since the PDMS hardly deforms.

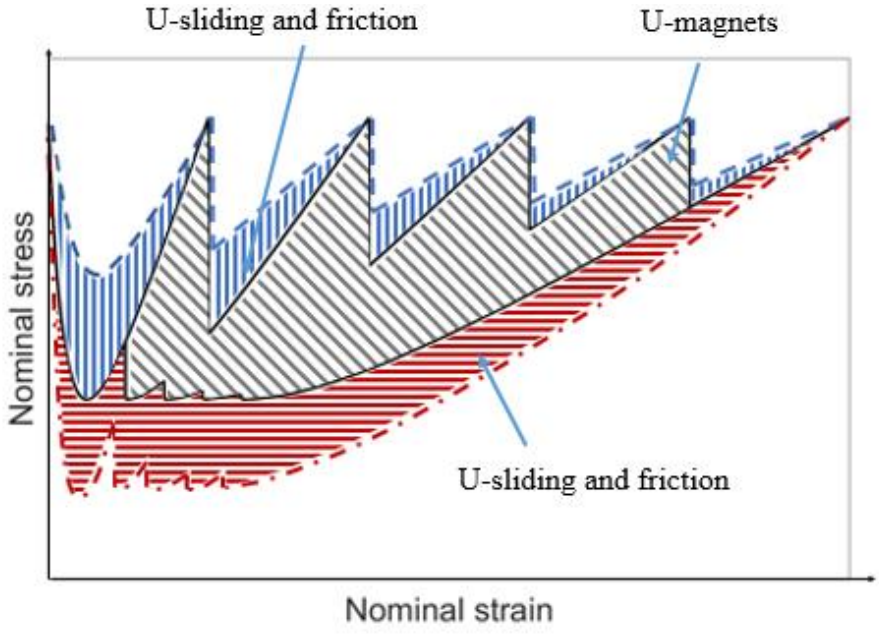

Figure 4.9. *Schematic sketch of actual loading and unloading curve above and under theoretical curve.*

From the schematic sketch in Fig. 4.9, we can see the actual loading curve should be above our thoretical curve. During unloading, we still have a frictionless curve which is uniform. For each unloading step, the strain is decreasing faster than the frictionless case since the magnets are kept in place due to friction. Thus, the unloading curve stays under the theoretical curve. Based on this analysis, we also plot loading and unloading curves based on our theoretical model.

4.4 Discussion

Similar to the PDMS-magnetic DN composite, the VHB magnetic composite exhibited clear toughening mechanisms. Instead of making a single magnetic chain composite, we build a new kind composite which contains multiple chain. For this sample, five chains of magnets are aligned in the loading direction while the 2nd and the 4th chain are intentionally put with half of magnet length mismatch.

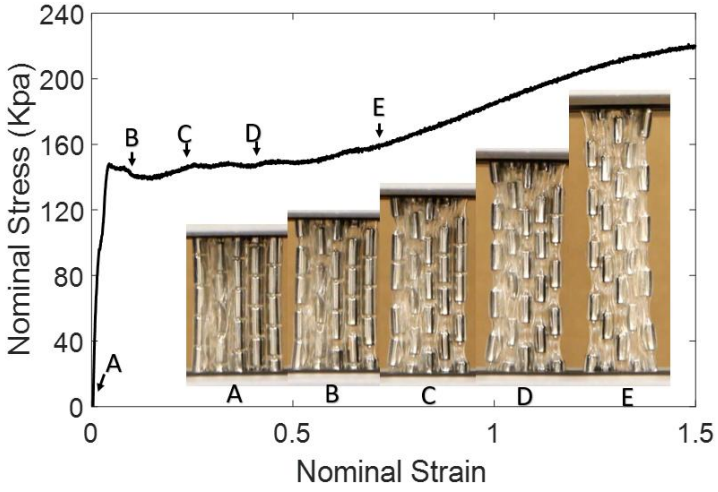

Figure 4.10. *Nominal stress-strain curves of a VHB-Magnet composite. The insets A – Eare the snapshots of the sample corresponding to the specific points along the loading curves. Over the stress plateau (A-E), partially damaged regions coexisted with the undamaged regions, and the extension was accompanied by the growth of the "damaged" regions. In the strain-hardening state, the entire magnet chain was separate, and the extension caused further sliding between magnets and VHB tape.*

The force-stretch curve of this VHB magnetic composite is shown in Fig. 4.10. The VHB magnetic composite shows similar curve with our PDMS magnetic composite. It also includes three stages, while the stick slip effect in the second stage are very smooth due to the mismatch aligned magnet chains. This serves as an illustration samples for the toughening mechanism on large scale composite.

4.5 References

[1] Gong, Jian Ping, et al. "Double-network hydrogels with extremely high mechanical strength." Advanced materials 15.14 (2003): 1155-1158.

[2] Gong, Jian Ping. "Why are double network hydrogels so tough?." Soft Matter 6.12 (2010): 2583-2590.

[3] Nakayama, Atsushi, et al. "High mechanical strength double-network hydrogel with bacterial cellulose." Advanced Functional Materials 14.11 (2004): 1124

[4] Yasuda, Kazunori, et al. "Biomechanical properties of high-toughness double network hydrogels." Biomaterials 26.21 (2005): 4468-4475.

[5] Illeperuma, Widusha RK, et al. "Fiber-reinforced tough hydrogels." Extreme Mechanics Letters 1 (2014): 90-96.

[6] Reichert, Werner Franz, Dietmar Göritz, and Edgar Johannes Duschl. "The double network, a model describing filled elastomers." Polymer 34.6 (1993): 1216-1221.

[7] Santangelo, P. G., and C. M. Roland. "The mechanical behavior of double network elastomers." Rubber chemistry and technology 67.2 (1994): 359-365.

[8] Ducrot, Etienne, et al. "Toughening elastomers with sacrificial bonds and watching them break." Science 344.6180 (2014): 186-189.

[9] Sun, Jeong-Yun, et al. "Highly stretchable and tough hydrogels." Nature 489.7414 (2012): 133.

[10] Azuma, Chinatsu, et al. "Biodegradation of high-toughness double network hydrogels as potential materials for artificial cartilage." Journal of Biomedical Materials Research Part A: An Official Journal of The Society for Biomaterials, The Japanese Society for Biomaterials, and The Australian Society for Biomaterials and the Korean Society for Biomaterials 81.2 (2007): 373-380.

[11] Haque, Md Anamul, Takayuki Kurokawa, and Jian Ping Gong. "Super tough double network hydrogels and their application as biomaterials." Polymer 53.9 (2012): 1805-1822.

[12] Tsukeshiba, Hiroyuki, et al. "Effect of polymer entanglement on the toughening of double network hydrogels." The Journal of Physical Chemistry B 109.34 (2005): 16304-16309.

[13] DeKosky, Brandon J., et al. "Hierarchically designed agarose and poly (ethylene glycol) interpenetrating network hydrogels for cartilage tissue engineering." Tissue Engineering Part C: Methods 16.6 (2010): 1533-1542.

[14] Rakovsky, A., et al. "Poly (ethylene glycol)-based hydrogels as cartilage substitutes: Synthesis and mechanical characteristics." Journal of applied polymer science 112.1 (2009): 390-401.

[15] Gong, Jian Ping. "Materials both tough and soft." Science 344.6180 (2014): 161-162.

[16] Keplinger, Christoph, et al. "Stretchable, transparent, ionic conductors." Science 341.6149 (2013): 984-987.

[17] Sun, Tao Lin, et al. "Molecular structure of self-healing polyampholyte hydrogels analyzed from tensile behaviors." Soft matter 11.48 (2015): 9355-9366.

[18] Sun, Tao Lin, et al. "Physical hydrogels composed of polyampholytes demonstrate high toughness and viscoelasticity." Nature materials 12.10 (2013): 932.

[19] Zhao, Xuanhe. "Multi-scale multi-mechanism design of tough hydrogels: building dissipation into stretchy networks." Soft Matter 10.5 (2014): 672-687.

[20] Feng, Xiangchao, et al. "A highly stretchable double-network composite." Soft matter 12.44 (2016): 8999-9006.

[21] Agashe, Janhavi S., and David P. Arnold. "A study of scaling and geometry effects on the forces between cuboidal and cylindrical magnets using analytical force solutions." Journal of Physics D: Applied Physics 41.10 (2008): 105001.Vokoun, David, et al. "Magnetostatic interactions and forces between cylindrical permanent magnets." Journal of magnetism and Magnetic Materials 321.22 (2009): 3758-3763.

[22] Vokoun, David, et al. "Magnetostatic interactions and forces between cylindrical permanent magnets." Journal of magnetism and Magnetic Materials 321.22 (2009): 3758-3763.

[23] Tang, X., Y. Chen, and H. Conrad. "Structure and interaction force in a model magnetorheological system." Journal of intelligent material systems and structures 7.5 (1996): 517-52

CHAPTER 5. FRACTURE OF DOUBLE NETWORK GEL

5.1 Introduction

Double-network (DN) gels have drawn much attention having both high mechanical strength and toughness while containing up to 90 wt% water.[1] But until now there isn't a very good model can illustrate the toughening mechanism and the fracture process of DN gel. To get a better understanding of what is happen during the fracture of DN gel, we need take a further look of the deformation process during loading of DN gel.

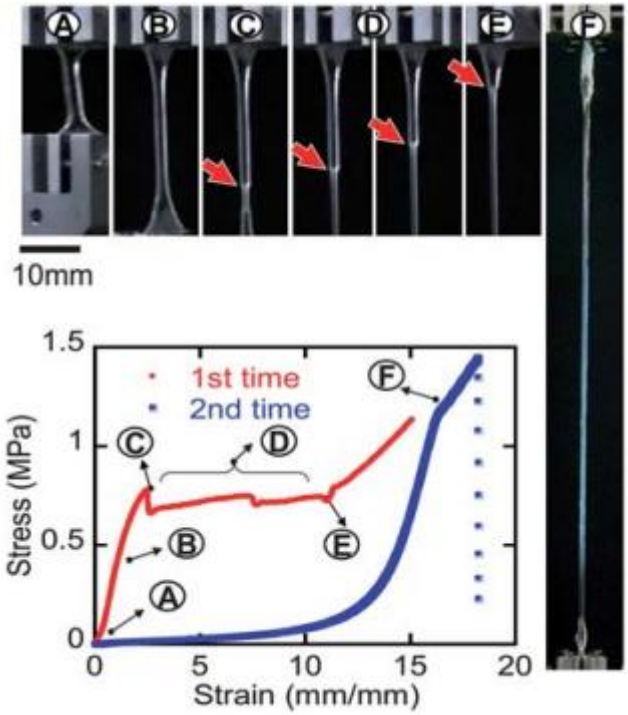

Figure 5.1. *Loading curve of a representative DN gel (PAMPS/PAAm DN gel) under uniaxial loading case, and pictures demonstrating the necking process. The insert alphabets represent the correspondence between the pictures and the arrowed data points.*

The yielding phenomenon has been found in several DN gels. Like metal, DN gels with fragile 1st network form narrowing zones in the sample during uniaxial tensile tests. As shown in Fig. 5.1, the 'Necks' continue to expand when the sample is further loaded. From

the stress-strain curve we can see a very obvious plateau region corresponding with the necking behavior as we mentioned before. This is a very interesting phenomenon since this is first found in gel systems reported by Gong's group. [2]. They also mention this plateau stress almost independent on the strain rate. When further loading until the grow ends, the DN gel become very soft and flexible, which could undergo extremely large stretch until fracture.

Experiment results also shows the PAMPS SN gel (1st network) are brittle and breaks at small stretch.[1] This serves as an evidence that the 1st network will first fragment into very small clusters and dissipate energy. When unloaded and loaded for 2nd or 3rd time tensile tests, the stress strain curves are quiet difference than the 1st time and all the following loading cycles have almost same loading curves. This indicates the large hysteresis of the 1st network fracture.

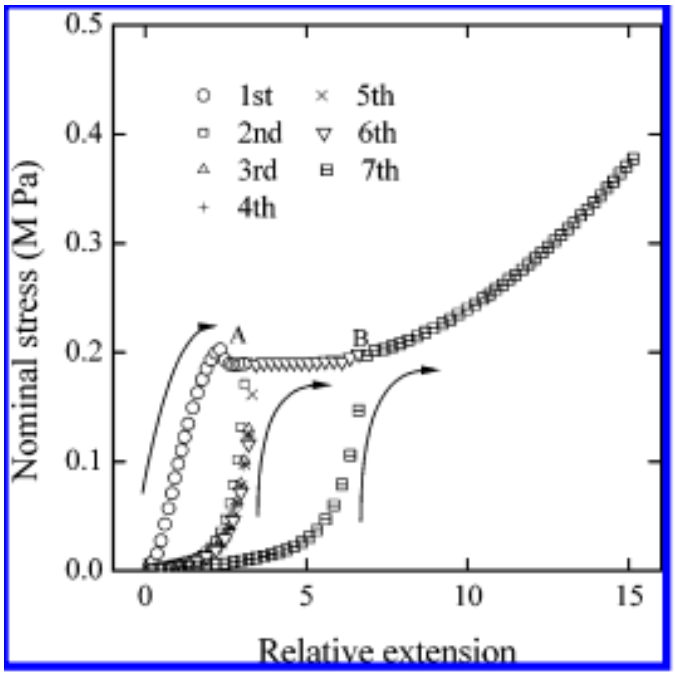

Figure 5.2. *Loading curves of DN gel for repeated loading cycles.*

It is also found irreversible structural change happens inside the gel after the tensile test finishes although the gel still looks the same. The boundary region between the necking zone and un-necking zone become opaque while the necking zone is still transparent.[2] This indicates the interior chemical structure of DN gel has changed and inhomogeneity with a characteristic size around visible light forms inside the boundary region. Some phase transformation phenomenon may have occurred in the DN gel system according to this experimental observation.

Overall, the fracture of DN gel shows two important features : the yielding behavior during elongation and some transformation happens at the necking zone. This reminds us the transformation toughening theory in some brittle materials. In the classic paper issuing the transformation toughening problem, a theory based on linear elastic approach is proposed. To some extent, the fracture of DN gel can be treated as a transformation toughening case at finite strain.

5.2 Transformation toughening theory

Transformation toughening corresponds to the fracture toughness enhancing behavior in a lot of ceramic systems with particles which undergo a stress-induced martensitic transformation. For examples, the zirconia particles transform from a tetragonal crystal structure to a monoclinic crystal structure at critical stress. The stress concentration near the crack tip induce the high stress which cause the transformation of particles. Obviously, the crack tip stress field has also been changed. When freely transformed, the particles could reach a shear strain about 16% and a dilation of 4% [3]. While embedded in the ceramic matrix, it becomes much smaller than 16% for shear strain while the dilation keeps the same.

Two groups of researchers, McMeeking and Evans[4], Budiansky and Hutchinson both formulated the continuum theory for transformation toughening. While, McMeeking's paper only take the dilatant part of transformation into account. So their prediction of the toughness increase are less than the corresponding experimental results. Budiansky's paper also neglect the shear component of the transformation. But the results are more comparable to the experimental results. Here, we pick the Budiansky and Hutchinsion's formulation for study.

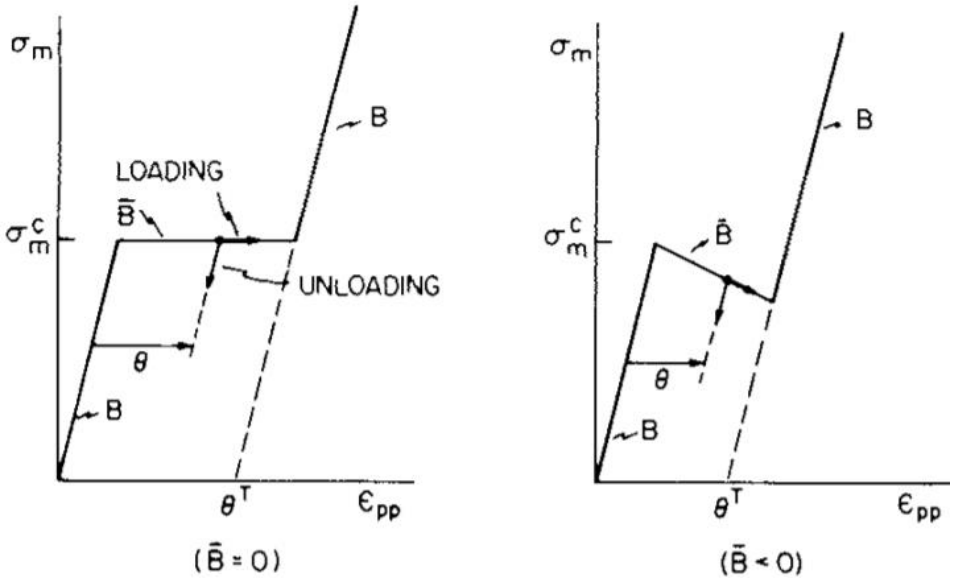

Figure 5.3. *Dilatant stress-strain behavior of the composite shows transformation toughening behavior. The right curve for* $\bar{B} < 0$ *shows some softening effect.*

This is a representative dilatant stress-strain behavior for the composite in this study. We can see the relation is very close to what we have seen in the behavior of DN gel. σ_m^c is the critical mean stress associated with the starting of the phase transformation of particles inside the composite matrix.

Here it is assumed the height of the transformation zone is small compared with the length of the crack. The asymptotic solution can be used for a semi-infinite crack under small scale transformation condition. The stress field apart from the crack tip is given by

$$\sigma_{ij} = \frac{K}{\sqrt{2\pi r}} f_{ij}(\phi),\ r \to \infty \tag{5.1}$$

where K is the elastic stress intensity factor which is controlled by the load. While at the crack tip the particles have been fully transformed and the stress field only differs in amplitude,

$$\sigma_{ij} = \frac{K_{tip}}{\sqrt{2\pi r}} f_{ij}(\phi),\ r \to 0 \tag{5.2}$$

K_{tip} governs the fracture processes at the crack tip. Therefore the increase from K_{tip} to K determines the toughening due to the transformation.

The unperturbed elastic solution to calculate the mean stress is given by McMeeking and Evans[4] after a calculation

$$\sigma_m = \frac{K(1+\upsilon)}{3}\left(\frac{\pi r}{2}\right)^{-1/2}\cos\left(\frac{\phi}{2}\right) \tag{5.3}$$

Equating (3) to σ_m^c, we can find the boundary of the transformation zone region

$$R(\phi) = \frac{2(1+\upsilon)^2}{9\pi}\left(\frac{K}{\sigma_m^c}\right)^2\cos^2\left(\frac{\phi}{2}\right) \tag{5.4}$$

At very small θ_T, the shape of the transformation zone can be get based on the elastic solution. The maximum height of the transformed loading zone should correspond to where its tangent is horizontal. So the height of the boundary is given

$$H = \frac{\sqrt{3}(1+\upsilon)^2}{12\pi}\left(\frac{K}{\sigma_m^c}\right)^2 \tag{5.5}$$

Based on these theories, several numerical examples have been studied by Budiansky and Hutchinson[3]. The transformed zone height and stress intensity factor ratio is plotted here in Fig. 5.4. It should be noted here that the original paper normalized the process zone size by a

increasing length scale, which made the comparison not straightforward. The process zone size in the original paper corresponds to $\bar{B} < 0$ case. They use α, corresponding to $\frac{\theta^T}{\theta^e}$, as a non-dimensional parameter. The issue here is that they didn't restrict α to be small. For large α values, the linear elastic condition might not work here.

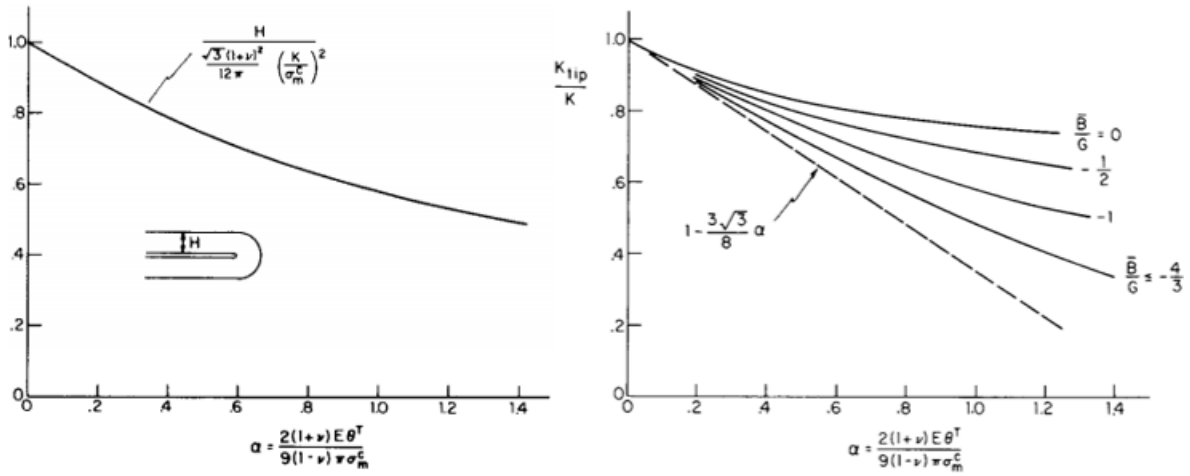

Figure 5.4. *Left: Height of transformation zone for $\bar{B} < 0$ transforming materials. Right: Ratio of near-tip to remote stress intensity factor.*

It is also found that for $\bar{B} = 0$ material, the larger transformation strain material will have only a small portion of process zone which is fully transformed. In general, we can treat the s-s curve of DN gel as a large scale transformation toughening case and we will compare the results with transformation toughening theory in following sections.

5.3 Phase field model of double network gel

The elastic energy of DN gel can be divided into two parts: the energy stored in the 1st network and the energy stored in the 2nd network. As pointed out, the 1st network is very fragile, while the 2nd network is much softer. Here, we introduce a strain induced damage

function $dmg[\max(I1) - 3]$ for the 1st network, as shown in Fig. 5.5. When the deformation of DN gel reaches the critical value of $\max(I1) - 3$, the 1st network starts to failing. Under further loading, the final failing of the whole 1st network finishes. As this is a homogenized material model, the random distribution of 1st network initial length and stretchability are all counted into the final failing point.

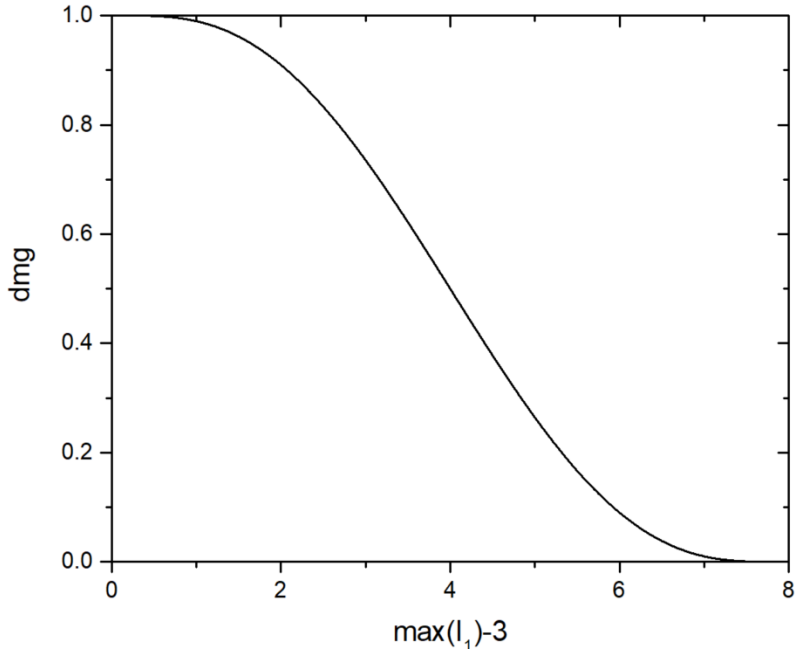

Figure 5.5. *Damage function dmg for the 1st network.*

Here, we use the neo-hookean model to describe the behavior of 1st network.

$$W_{1st} = \frac{\mu_{1st}}{2}(I1 - 3) \tag{5.6}$$

The 2nd network is soft and stretchable, with some stiffening effect at very large stretch before failing. Yeoh's model is a good candidate to formulate the stress strain relation of 2nd network.

$$W_{2nd} = \frac{\mu_{2nd}}{2}[(I1 - 3) + C_2(I1 - 3)^2 + C_3(I1 - 3)^3] \tag{5.7}$$

The elastic energy density function of the DN gel can be written as the following

$$W_e = dmg[max(I1) - 3]W_{1st} + W_{2nd} \tag{5.8}$$

The elastic energy density function of the DN gel for different damage stage are plotted in Fig. 5.6. As the 1st network starts to damage, the energy function goes to the right curve.

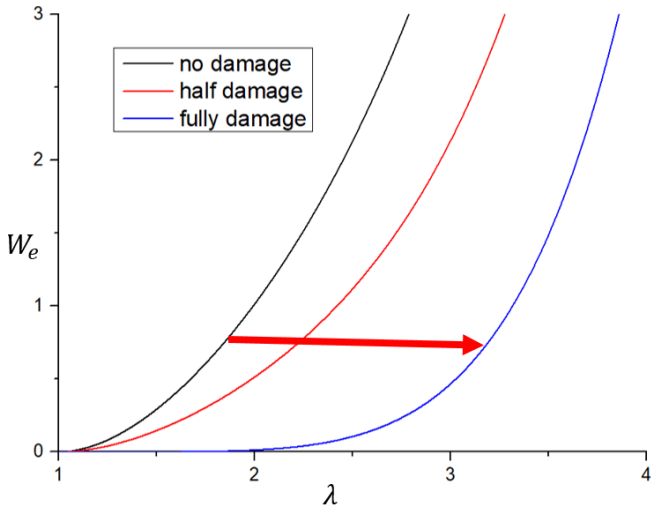

Figure 5.6. *The elastic energy density function of the DN gel under uniaxial elongation deformation λ for different damage stage.*

It should be noted here there exists an unstable part of the elastic energy of DN gel. Here by taking partial derivative of W_e over λ, we can get the stress-stretch relation, as shown in Fig. 5.7. The negative stress part corresponds to the unstable part in the elastic energy plot. This is because our model is for perfect material, which means there isn't any defect inside the chemical structure. This kind of material model needs to nucleate a necking zone first and then yield. For real DN gel systems, there is always some weak 1st network or defects in 1st network, so the peak point of the elastic energy will drop or disappear. From the curve we can see that our DN gel model are more close to $\bar{B} < 0$ transformation system.

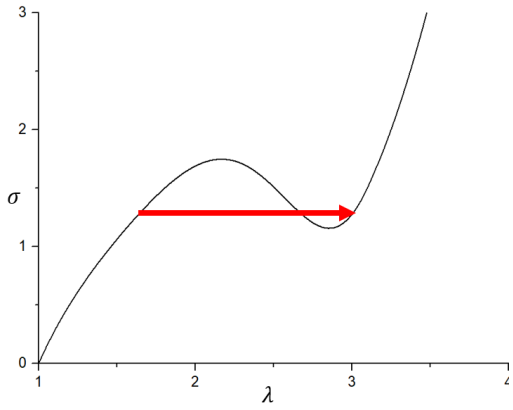

Figure 5.7. *The stress-stretch relation of the DN gel under uniaxial elongation stretch λ.*

Here we set the shear modulus of 1st network equals to 1 and varies the shear modulus of 2nd network from 0.5 to 0.0005. We successfully create a bunch of stress strain curves with the same normalized yielding stress 0.75, which is shown in Fig. 5.8. The stress is normalized by the shear modulus of the 1st network. The resulted transformation strain for the whole set stress strain curves increases from 15% to 400%.

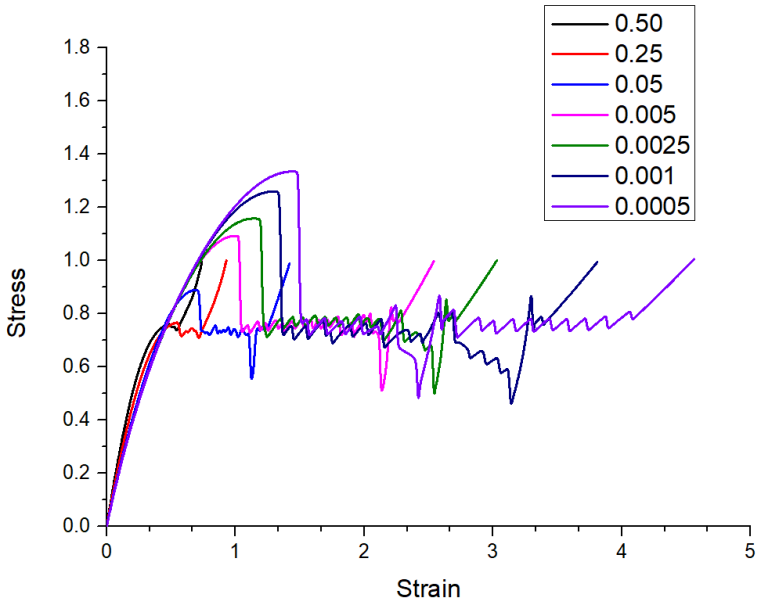

Figure 5.8. *The normalized stress-stretch curves of the DN gel for numerical study. The number in the legend corresponds to the shear modulus of 2nd network. The stress is normalized by the shear modulus for the 1st network, which is 1.*

Following the same formulation of previous phase field model, we write the free energy density function at finite strain as

$$W = dmg[max(I1) - 3]W_{1st} + g(\phi)W_{2nd} + g(\phi)W_c + \frac{\kappa}{2}(\nabla\phi)^2 \qquad (5.9)$$

As we mentioned before, the 2nd network hold the integrity of the DN gel structure, so we write the phase field damage function with the 2nd network elastic energy term. In this study, we choose the interpolant $g(\varphi) = 1 - 3\varphi^2 + 2\varphi^3$. Now the intact region ($\varphi = 0$) and a fully damaged region ($\varphi = 1$) is the other around with previous study.

In Chapter 2 we have already done the nondimensionalization of the phase field formula, which we will not do it again here. But it is worthy to mention that the intrinsic length scale $r = \sqrt{\kappa / W_c}$ here is approximately the thickness of the transition zone from the intact region to a full damaged region for 2nd network. While the intrinsic fracture energy of the material $\Gamma \approx 2\sqrt{\kappa W_c}$ is corresponding to the fracture energy of 2nd network as well. In experiments, the toughening factor of DN gel is also measure with the fracture energy of the Single-Network gel system consisting 2nd network only.

To enforce volume incompressibility, we use a similar approach by adding to the free energy function a term with a Lagrange multiplier p representing the pressure field. As we pointed out in previous section, a physically meaningful model needs to degrade the compressibility simultaneously with the shear stiffness. Directly multiplying the Lagrange multiplier term by $g(\phi)$ obviously does not serve the purpose. Instead, we modify the Lagrange multiplier term slightly by modeling the material as slightly compressible:

$$-pg(\varphi)(1-\phi)^4 - \frac{p^2}{2}\phi^2 \qquad (5.10)$$

By taking the variation of (4) with respect to p, one will arrive at an equation of state with a degrading bulk modulus: $p = -\frac{(1-\phi)^4}{\phi^2}(\det \mathbf{F} - 1)$. In the intact state $\varphi = 0$, the pressure $p \to \infty$ ensures volume conservation; in the fully damaged state $\varphi = 1$, $p = 0$.

5.4 Results and discussion

The phase field model of DN gel is implemented into Comsol Multiphysics 5.3. The numerical simulation has successfully reproduced the process zone of the 1st network and the crack of the whole material. The results in reference state and current state are shown in the Fig. 5.9. The reference state also corresponding to the state under which the material is unloaded from the current state.

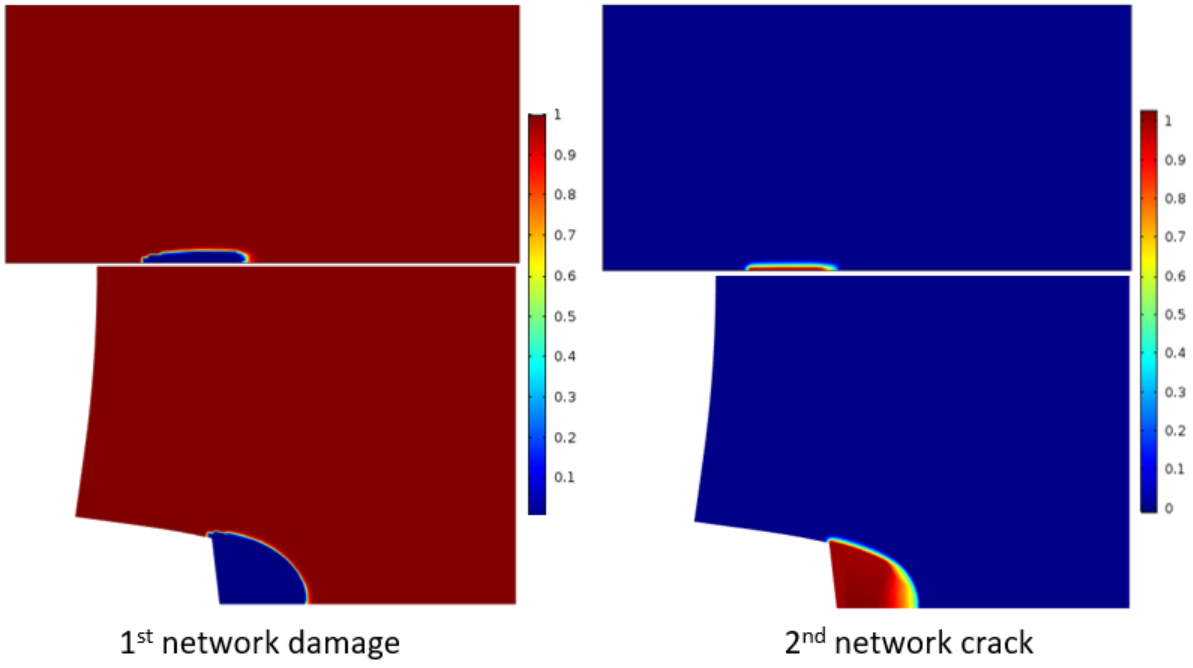

Figure 5.9. *The damage zone field for 1st network and crack field for the whole structure. Both in undeformed state and current state.*

For each case, we can measure the process zone size in the un-deformed state. For DN gel, we normalized the process zone size by the intrinsic length scale r of phase field model. For transformation toughening case, we rebuild the curves from the Budiansky and Hutchinson's paper and reformulated the x-axis into $\frac{\theta^T}{\theta^e} = \frac{\theta^T}{\frac{\sigma_m^c}{B}}$. It should be mentioned here that the length scale we use for transformation toughening is different with the original paper. Since Budiansky's paper referred to length related with K as the length scale. While for different cases, the stress intensity factor K has different value. Instead of using K, we take the length related with K_{tip} as the length scale, which keep the same for all the cases.

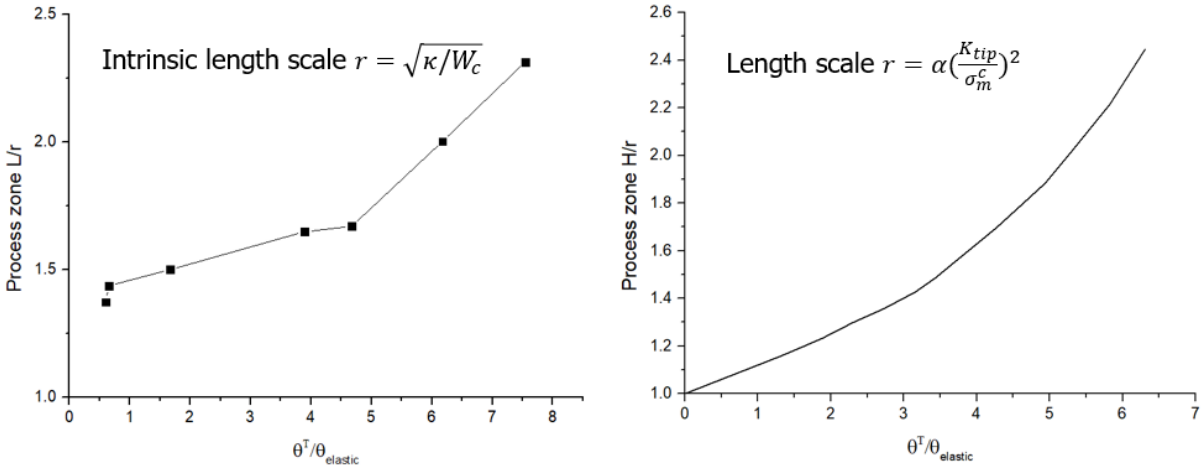

Figure 5.10. *Left: The process zone size of fracture of DN gel. Right: The transformation zone size of transformation toughening.*

It should be noted here that our θ^e is much larger compared with transformation toughening theory since the theory is based on linear elastic fracture mechanics. For the particles inside the matrix, they will start transformation at very small strain. While for the 1st network, despite its brittle behaviour, it still can carry much larger stretch than the metal particles. The model we used is a finite strain phase field model. From Fig. 5.10, we can see

there are some difference exists, but the overall trend of the increase of the length scale is comparable with traditional theory.

Another important result, the toughening factor which is the ratio between the overall fracture energy and the intrinsic fracture energy are plotted in Fig. 5.11. The blue line ($\bar{B} = 0$) refers to the stress strain relation as shown in Fig. 5.3, where no hardening or softening appears during elongation. The transformation comes with stress softening are marked in the red line ($\bar{B} < 0$).

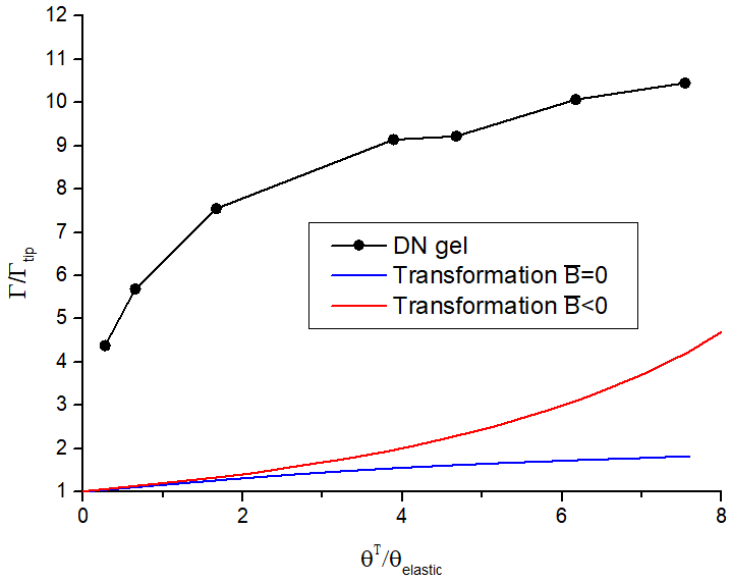

Figure 5.11. *The toughening factor, the ratio between the overall fracture energy and the intrinsic fracture energy.*

We'd first like to talk about the reason why the toughening factor difference is becoming less as the transformation increase. As the transformation strain increase from very small strain, the hysteresis energy in DN gel is initially much larger compared with classical transformation toughening stress strain relations, as shown in Fig. 5.12. While the difference

is becoming less and less this is due to under relatively large transformation strain, the classical theory has much large dissipation energy compared with DN gel.

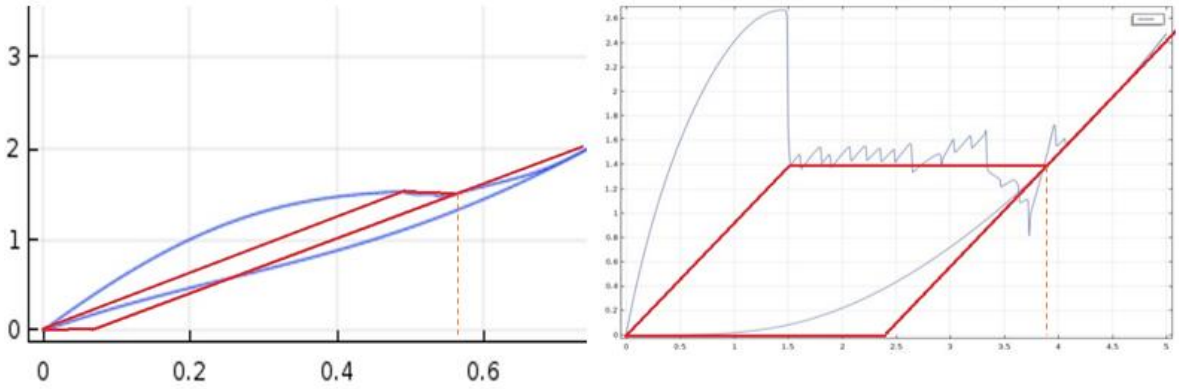

Figure 5.12. *Illustration of the difference of toughening factor between fracture of DN gel and transformation toughening. The stress-strain curves are shown for very small transformation strain on the left and large transformation strain on the right. The Blue line marks the fracture of DN gel while the red line marks the transformation toughening.*

There are several points worth talking about: (1) Budiansky and Hutchinson's paper [3] only consider the dilatant part of the transformation and omitted the shear strain of the transformation. Since the shear deformation of the transformation will accommodate some of the deformation in pure shear test, underestimation of the overall toughness does exist. (2) Our model is based on damage, while their model is based on transformation. These two approach already have lot of difference. The classic transformation toughening paper can just be a reference for our results, but we can't compare with it directly.

Finally, we can also get the scaling relation for the fracture energy of DN gel with the hysteresis energy between the loading and unloading curve. The results between the dimensionless fracture energy and dimensionless hysteresis energy are plotted by log-log scale in Fig. 5.13. The fracture energy is normalized by rW_c while the hysteresis energy is normalized by W_c. We fit the simulation results points and derive the scaling law for the

fracture energy of double network gel to be proportional to the hysteresis energy to the power around 0.52.

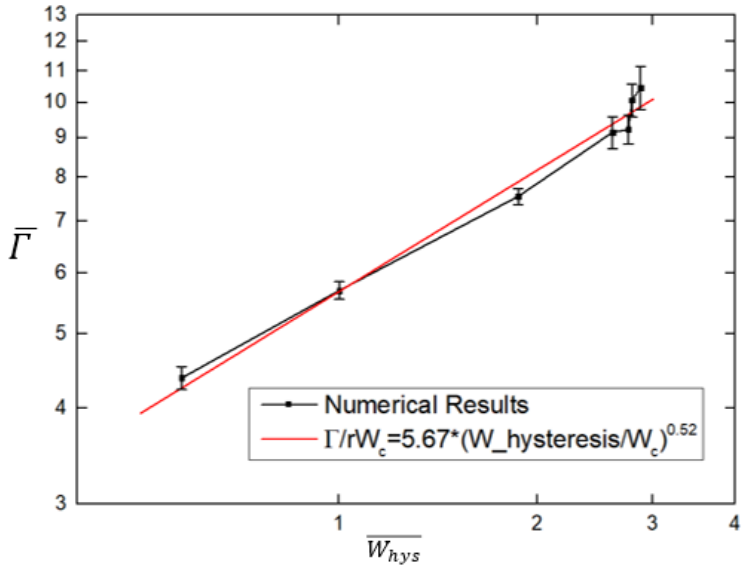

Figure 5.13. *The relation between dimensionless fracture energy of DN gel* $\bar{\Gamma}$ *and the dimensionless hysteresis energy between the loading and unloading curve* $\overline{W_{hys}}$.

As the transformation strain increases, the process zone shape after unloading changes significantly. The snapshot of the process zone for three different transformation strain are plotted in Fig. 5.14. The red line marks the crack of the whole material. The process zone length ahead of the crack tip increase as the transformation strain raises. It can be understood in this way: The outside region which is not damaged is limited by the maximum deviatoric strain through the damage function. The deformation under pure shear test is related with the damage zone slope, larger slope corresponding to larger deviatoric strain. For the larger transformation strain case, the final process zone opening is larger in deformed state. With the same slope, it need longer depth of process zone to accommodate the large deformation. Also, the unloaded process zone will be much longer than the

deformed state due to the incompressibility of the material. This explains why the process zone shape changes in this way.

For our DN gel model, $\bar{B} < 0$, the result show larger portion of the process zone is fully damaged. Actually these 2 configuration have very large difference while for linear elasticity, very small difference. At crack tip, the material is more like have dilation strain but other places the classic theory omit.

Furthermore, our model is a homogenized model. The damaged process zone doesn't mean the damage is everywhere. It could be some part or some island of the 1st network is damaged inside this zone. In Fig. 3.5, the sibling damage of the 1st network (fabric mesh) ahead of the crack tip is a good example for the process zone shape [5].

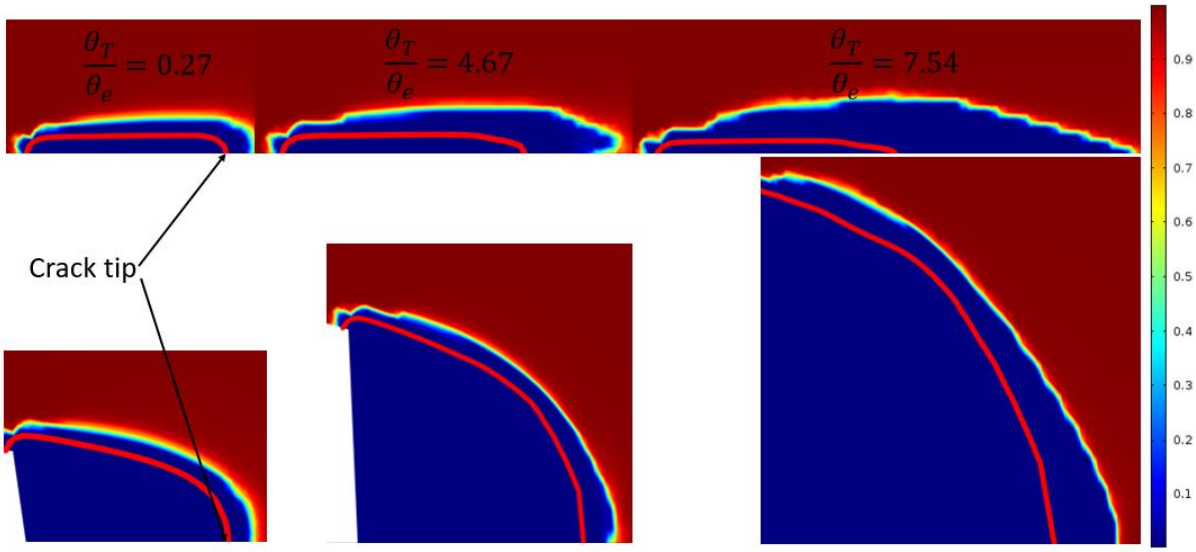

Figure 5.14. *The process zone in reference state and current state for three cases,* $\frac{\theta_T}{\theta_e} = 0.27$, $\frac{\theta_T}{\theta_e} = 4.67$ *and* $\frac{\theta_T}{\theta_e} = 7.54$. *The red line corresponds to the crack.*

The DN gel system usually shows 100-1000 times fracture energy increase compared with that of SN gel made of 2nd network. While our model predicts the toughening ratio

significantly lower. Recent studies [6-8] have shown that the fatigue threshold energy is one or two order of magnitude lower than the fracture energy. For fatigue behavior, the material excludes the energy dissipation from the 1st network damage induced friction or sliding. Our model is a quasi-static model, these dynamic effects have not been taken into account. So our scaling law predicts the fatigue threshold fracture energy.

5.5 Conclusion

The experimental results for fracture of DN gel is reviewed. Showing similarity with the fracture of DN gel, the continuum transformation toughening theory is discussed and reviewed. A material model for DN gel and related phase field model for the fracture of DN gel is proposed. Several representative stress strain curves of DN gel are built and the numerical results are compared with transformation toughening. The process zone and the toughening factor shows the similar trend with transformation toughening results. A scaling relation between the fatigue fracture energy of DN gel and the hysteresis energy of DN gel is proposed. The process zone shape difference is found through our numerical simulation while no current experimental results have found. The relation between the portion of fully damaged material in the process zone with transformation strain is discussed.

5.6 References

[1] Gong, Jian Ping. "Why are double network hydrogels so tough?." Soft Matter 6.12 (2010): 2583-2590.

[2] Na, Yang-Ho, et al. "Necking phenomenon of double-network gels." Macromolecules 39.14 (2006): 4641-4645.

[3] Budiansky, B_, J. W. Hutchinson, and J. C. Lambropoulos. "Continuum theory of dilatant transformation toughening in ceramics." International Journal of Solids and Structures 19.4 (1983): 337-355.

[4] McMeeking, R. M., and A. G. Evans. "Mechanics of transformation-toughening in brittle materials." Journal of the American Ceramic Society 65.5 (1982): 242-246.

[5] Feng, Xiangchao, et al. "A highly stretchable double-network composite." Soft matter 12.44 (2016): 8999-9006.

[6] Zhang, Wenlei, et al. "Fatigue of double-network hydrogels." Engineering Fracture Mechanics 187 (2018): 74-93.

[7] Bai, Ruobing, et al. "Fatigue fracture of tough hydrogels." Extreme Mechanics Letters 15 (2017): 91-96.

[8] Tang, Jingda, et al. "Fatigue fracture of hydrogels." Extreme Mechanics Letters 10 (2017): 24-31.

CHAPTER 6. CONCLUSION

In summary, we have advanced the field of fracture and deformation of soft materials and structures in the following aspects:

Drawing an analogy between the compliant ligaments in a soft elastic foam and the polymer chains in an elastomer, we propose a polymer-network-like toughening mechanism and derives the scaling relation between the macroscopic fracture energy and the structural characteristics of soft foam structures. Different from the energy absorbing mechanism of rigid foams which is mainly effective at compression, the polymer-network-like toughening mechanism allows a soft foam to effectively dissipate energy when the structure is subject to tension. Through a phase-field model developed specifically for the fracture of elastomers, the toughening mechanism as well as the scaling relation is then verified on soft foam structures of various geometries. In addition to the scaling law, it is found that the geometric parameters such as the ligament density and the network connectivity will also affect the fracture energy of soft foams. Finally, to increase the volume fraction of the solid phase without affecting the thickness or slenderness of each ligament, a type of soft foam structures of serpentine ligaments is proposed. Numerical study suggests that such structures may reach an effective fracture energy much higher than that of the corresponding bulk material. In other words, one may toughen a soft material just by cutting slots or holes in it.

By using a fabric mesh and a VHB acrylic tape, a soft but highly stretchable DN composite was manufactured and its mechanical properties tested. The DN composite followed very similar damage-distribution and toughening mechanisms as in the well-known DN hydrogels: it exhibited a stable necking phenomenon during uniaxial tension, it possessed large hysteresis during cyclic tensile tests and dissipated significant amount of

damage, and it showed good crack tolerance. The DN composite was as strong as the mesh, as stretchable as the tape, and significantly tougher than either materials. The deformation and damage evolution process in the DN composite can be divided into three stages: the initial elastic stage prior to any damage, the stress plateau stage corresponding to the damage propagation in the mesh layer, and the strain-hardening stage in which the deformation is manifested mainly by interlayer sliding. To capture the damage evolution process and to better understand the toughening mechanism, a theoretical model is developed by assuming 1D deformation and damage. The finite interlayer sliding is represented by a shear-lag model. With very few parameters obtained from independent tests over the base materials, the theory predicts the stress-stretch curves that agree well with the experiments in all compositions. The DN composite, on the other hand, can be regarded as a macroscopic model for the study of DN hydrogels. Through visualizing the damage evolution and correlating the macroscopic properties with the underlying structures, it may provide insights towards the further optimizing of DN hydrogels for enhanced properties.

Inspired by the salient self-healing capabilities of the ionic crosslinks in the tough gels, we designed and tested a magnetic DN composite capable of large and recoverable deformation in this work. In analogy to the reversible ionic crosslinks in self-healing hydrogels, permanent magnets were used as the sacrificial and reconnecting components in the composite. The magnets were initially connected into fibers which provided the composite relatively high stiffness. Under a critical axial tension, the magnets separated from each other in sequence, and transferred the load to the elastomeric matrix. Exhibiting a long plateau over the stress-strain curve, the damage evolution process was similar to that of DN gels and elastomers. The strength of the composite was limited by the magnetic

attractions while the maximum stretch was limit by the stretchability of the matrix. The composite was significantly tougher than either of the constituents. Upon unloading, the magnetic attraction between neighboring magnetics held them back again and the composite's stiffness and strength were fully recovered. A simple 1D model is proposed and the theoretical stress strain curve is reproduced. By introducing the concept of sliding and friction, the difference between theoretical curve and experimental curve has been explained.

A material model for DN gel and related phase field model for the fracture of DN gel is proposed. The fracture of DN gel is first compared with transformation toughening theory. Several representative stress strain curves of DN gel are built and the numerical results are compared with transformation toughening. The process zone and the toughening factor shows the similar trend with transformation toughening results. A scaling relation between the fracture energy of DN gel and the hysteresis energy of DN gel is proposed. The process zone shape shows similar pattern with what we observed in DN composite experiments.